ORIGINAL PAPER

Probing Wave Functions of Electrically Active Shallow Level Defects by Means of High-Frequency Pulsed ENDOR in Wide Bandgap Materials: SiC, AlN, ZnO, and AgCl

S. B. Orlinskii, et al. *[full author details at the end of the article]*

Abstract

In the high-frequency ENDOR experiments, the hyperfine (HF) interaction between the unpaired electron of the shallow donor or shallow acceptor and the nuclear spins of the Coulombic center and the surrounding atoms is determined, which is then translated into the spin density of the electronic wave function at the various atomic positions. The results of studying the spatial distribution of wave functions for shallow donors in ZnO, AgCl, AlN, and SiC crystals, ZnO-based nanostructures, and shallow boron acceptors in SiC will be presented. The change of the electronic wave function of a shallow donor in ZnO quantum dots (QDs) when entering the regime of quantum confinement by using the nuclear as probes has been observed. The model, based on the effective mass approximation (EMA), that describes a 1s-like wave function with the Bohr radius of ~1.5 nm for distant shells was tested. The EMA does not yield an appropriate description of the electronic wave function when the radius of the QD is reduced below the Bohr radius. The direct reconstruction of the wave function of the intrinsic shallow electronic center (SEC) and self-trapped excitons in AgCl was presented. The SEC was suggested to be an electron that is shallowly trapped by two adjacent silver ions on a single cationic site (split-interstitial position), so-called "latent image" in silver halides. The shallowly trapped electron of the STE is shown to behave like a hydrogen $1s$ electron, centered on the Ag^+ lattice position, with a Bohr radius $r_0 = 1.51$ nm that is in agreement with Bohr radius of SEC ($r_0 = 1.66$ nm). For SEC in AgBr, $r_0 = 2.48$ nm. It was demonstrated that dynamic nuclear polarization of nuclear spins due to hyperfine interactions with ligand nuclei can be achieved in ZnO (and based QDs) and AgCl by saturating the high-frequency EPR transition of a shallow donor at low temperatures corresponding to a high Boltzmann factor. Several types of shallow donors were indicated in AlN crystals: (i) affected by the DX-relaxation and (ii) with normal behavior. The strong HF interaction for light-induced SD in AlN support the assignment to the impurity in anionic sublattice (e.g. oxygen in N position). At the same time, a shallow donor with normal behavior can belong to Si or C in the Al position. The electronic structure of shallow donors and shallow acceptors in silicon carbide was investigated by the ENDOR method. The spin density of the N donor corresponding to the observed

ENDOR lines was established to be *p* like in character and located mainly on the Si atoms for the k site in 4H-SiC, whereas for the three sites in 6H-SiC the spin density is s-like in character and located mainly on the C atoms. An explanation for the difference in the electronic wave function of the N donor in 4H-SiC and 6H-SiC can be found in the large difference in the band structure of the two polytypes and in the position of the minima in the Brillouin Zone. The electronic density for shallow B acceptor substituting Si in the *k* position is distributed in an ellipsoidal shape with the main symmetry axis making an angle of 70° with the c axis, i.e., along the direction of the B–C with main spin density.

1 Introduction

Obtaining information on the electronic spatial distribution of electrically active shallow donors and acceptors in semiconductors, diagnostics of their structure and chemical identification is a fundamental problem in the physics and technology of semiconductors. Electron paramagnetic resonance (EPR) and electron-nuclear double resonance (ENDOR) are the methods of choice for such studies. In the ENDOR experiments, the hyperfine (HF) interaction between the unpaired electron spin of the donor or acceptor and the nuclear spin of the surrounding atoms is determined, which is then translated into the spin density of the electronic wave function. The review is devoted to the use of high-frequency pulsed EPR and ENDOR methods for studying electrically active donor and acceptor impurities with shallow levels in wide-band-gap semiconductors of IV–IV, III–V, II–VI, and I–VII groups. In the development of these methods and the experimental technique, a great role was played by the pioneering works of professors Kev M. Salikhov [1] and Klaus Möbius [2].

The EPR and ENDOR experiments were performed at temperatures ranging from 1.2 to 10 K using pulsed EPR spectrometers operating at 95 GHz [3] and 275 GHz [4]. The huge advantage of working at a large microwave frequency is that a high spectral resolution is obtained in the EPR as well as in the ENDOR spectra. In addition, the use of pulsed microwave techniques facilitates considerably the observation of the ENDOR spectra. The EPR spectra were recorded by monitoring the electron spin echo (ESE) signal following a microwave π/2- and a π-pulse sequence as a function of the magnetic field. The ENDOR spectra were obtained by monitoring the intensity of the stimulated echo, following three microwave π/2-pulses, as a function of the frequency of a radio-frequency (RF) pulse applied between the second and third microwave pulses (Mims ENDOR) [5].

The great potential of magnetic resonance spectroscopy can be realized in a combination of the continuous-wave (CW) EPR and pulsed EPR. The advantage of studies in a pulsed mode is the possibility to explore not only spin dynamics but also photoexcited paramagnetic species including paramagnetic excited states (e.g., excitons). ENDOR technique is very useful in systems with unresolved hyperfine structure and makes possible the detection of nuclear magnetic resonance (NMR) through its effect on the EPR signal, thus using a high EPR sensitivity as compared with the NMR. The hyperfine coupling constants could be measured with much

higher precision as compared with the EPR. Direct information about the spatial distribution of the wave function of unpaired electrons can be obtained from ENDOR measurements. This aspect is particularly attractive because it allows quantitative measurement of the confinement effect induced by the shape and properties of the wave function in quantum dots (QDs). A general feature of the band structure of the IV–IV, III–V, II–VI and I–VII semiconductors is a conduction band with predominantly s-like symmetry and a valence band derived from p-like atomic orbitals.

The results of studying the spatial distribution of wave functions and hyperfine (HF) interactions with the nuclei of impurity and ligand atoms for shallow donors in ZnO, AgCl, AlN, and SiC crystals, ZnO-based nanostructures, and shallow boron acceptors in SiC will be presented. It is shown how shallow donors in ZnO and AgCl provide dynamic polarization of nuclei due to hyperfine interactions with ligand nuclei.

2 Shallow Donors in ZnO Single Crystals and Based Quantum Dots

Zinc oxide (ZnO) semiconductor with a direct band gap of 3.3–3.4 eV, attracts considerable attention. The group III elements (Al, Ga, and In) substituting Zn atoms are expected to be shallow donors (SDs) in the ZnO single crystals. Indeed, by using EPR spectroscopy, In and Ga shallow donors were identified on the basis of the resolved hyperfine (HF) splitting observed in their EPR spectra. However, since such a hyperfine splitting is absent in the EPR signals of Al-doped ZnO single crystals, the identification of Al as the core of the shallow donor has not been unambiguously ascertained. The nature of shallow donors in nominally undoped ZnO crystals has not been clarified either. The results of the ENDOR studies of shallow donors in ZnO single crystals and based nanostructures were presented in Refs. [6–17].

By means of W-band (95 GHz) EPR and ENDOR studies [14], it was demonstrated that interstitial hydrogen acts as a shallow donor in nominally undoped ZnO, thus confirming the prediction of Van de Walle [18]. The experimental evidence was provided by the observation of the ENDOR signals of the nuclear spin of ^{1}H ($I = 1/2$) in the EPR signal possessing g factor of the shallow donor ($g \approx 1.95$).

Figure 1a shows optically-induced EPR spectra of SDs in undoped ZnO single crystal and Li-doped ZnO quantum dots (QD) measured at 94.9 GHz and $T = 1.5$ K using $\pi/2 - \tau - \pi$ microwave pulse sequence. QDs of the same core/shell structure ZnO/Zn(OH)$_2$ but with different radius R (3 nm, 1.73 nm, and 1.17 nm) are studied. The hat from "*The Little Prince*" by *Antoine de Saint-Exupéry*, symbolizes the hidden nature of the unresolved single EPR line. The non-resolved ESE-detected EPR spectra of shallow donors in ZnO single crystal measured in two different extreme orientations $B \| c$ ($g\| = 1.9569$) and $B \perp c$ ($g_\perp = 1.9552$) are presented in Fig. 1a.

In addition, Fig. 1a shows the non-resolved ESE-detected EPR spectra of shallow donors in ZnO QDs in the same magnetic-field scale. The g-factor shifts toward the free-electron value ($g = 2.00$) with decreasing in the size of the nanoparticles. This is caused by the confinement of the hydrogen-like 1 s-type wave function of shallow donors when the Bohr radius becomes comparable to the size of the QD. The c axis in a QD powder is randomly oriented and linewidth of

about 3–4 mT might be expected. Additional broadening of the EPR line can be
due to the size dispersion of about 10% in the ZnO QDs studied. The EPR spectra
in Fig. 1a do not provide information on the chemical nature of the donor since
no resolved hyperfine structure is observed. To identify the binding core, ENDOR
experiments are needed.

The ESE-detected ^{1}H ENDOR spectrum of the hydrogen-related shallow donor
in ZnO single crystal in two orientations $B\|c$ and $B\perp c$ are shown in Fig. 1b. Two
ENDOR lines symmetrically placed around the nuclear Larmor frequency of ^{1}H
separated by 1.4 MHz are observed. These lines are isotropic and correspond to a
hyperfine interaction (HF) constant $A = 1.4$ MHz. Thus, H is located in one well-
defined position within the electron wave function of the shallow donor and not at
random positions. Figure 1b shows that the two ENDOR transitions have opposite
signs. As shown in Ref. [19] it means that the sign of the HF interaction is positive
and caused by direct spin density on the H nucleus. Thus, the transparent hat from
"*The Little Prince*" by *Antoine de Saint-Exupéry* symbolizes the effectiveness of the
ENDOR method in determining the hyperfine interactions, hidden under the unre-
solved line.

The ENDOR spectrum of the ^{67}Zn nuclei ($I = 5/2$, abundance 4.1%) at frequen-
cies higher than the ^{67}Zn Larmor frequency is presented at the top of Fig. 1c. The
pulse sequence used in the experiment is the $\pi/2 - \tau - \pi/2 - T - \pi/2$ stimulated
echo sequence with radio-frequency pulse during the interval T (see Fig. 1d). The
pulse lengths are $\pi/2 = 150$ ns, $\tau = 400$ ns. The typical RF pulse length is $T = 100$ μs.
The ENDOR signals originate from of the ^{67}Zn nuclear spins that have an isotropic
hyperfine interaction with the unpaired electron spin of the shallow donor. The mul-
titude of ^{67}Zn nuclear-spin resonance lines, showing HF interactions ranging from
$a = 2.4$ MHz to $a = 0.01$ MHz, is caused by the fact that the electronic wave func-
tion is distributed in the crystal according to the 1 s-type wave function with a Bohr
radius of ~ 1.5 nm [14].
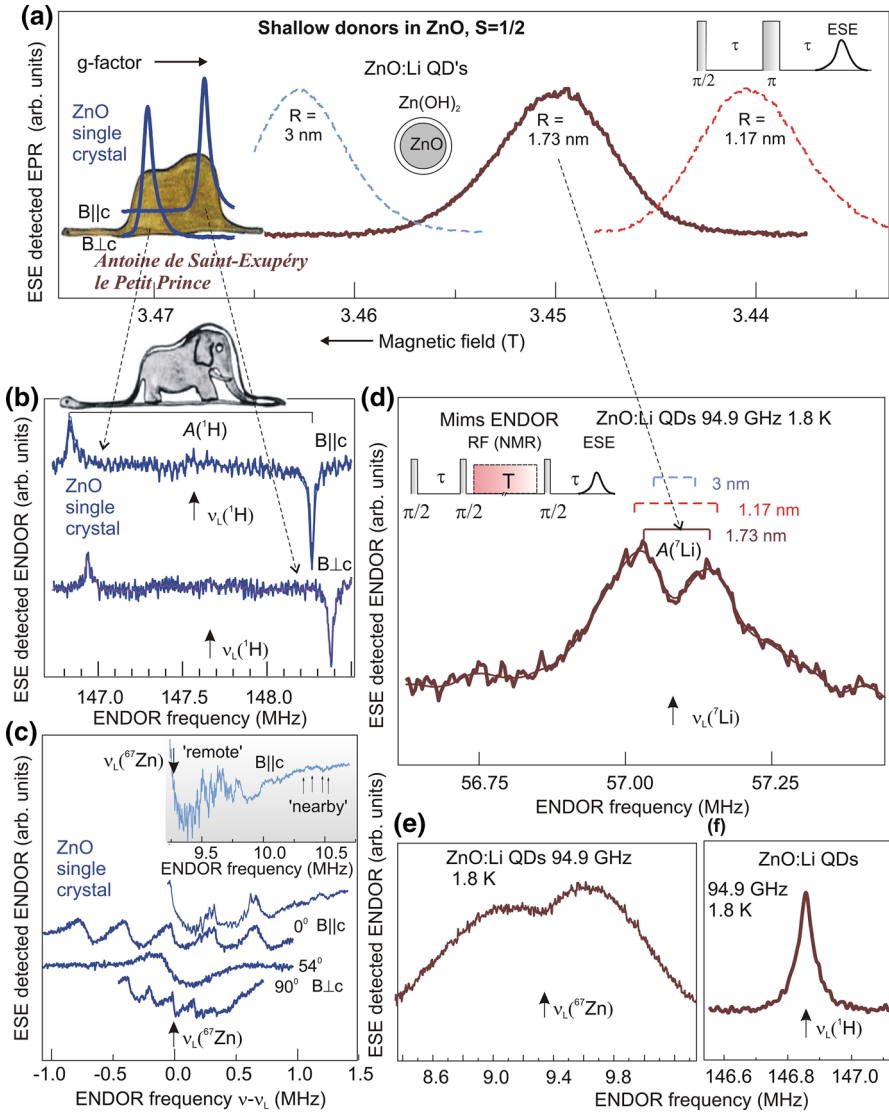
The EPR and ENDOR data for the shallow donors in ZnO can be described by a spin-Hamiltonian of the following form with $S = 1/2$:

$$\hat{H} = \mu_B \mathbf{S} \cdot \mathbf{g} \cdot \mathbf{B} + \mathbf{S} \cdot \mathbf{A_C} \cdot \mathbf{I_N} - g_{nC}\mu_N \mathbf{I_C} \cdot \mathbf{B} + \mathbf{I_C} \cdot \mathbf{P_C} \cdot \mathbf{I_C} - \Sigma(\mathbf{S} \cdot \mathbf{A_i} \cdot \mathbf{I_i} + \mathbf{I_i} \cdot \mathbf{P_i} \cdot \mathbf{I_i} - g_{ni}\mu_N \mathbf{I_i} \cdot \mathbf{B}).$$

(1)

where, $\mathbf{g}$ is the electronic g tensor, μ_B is the Bohr magneton and μ_N is the nuclear magneton; $\mathbf{A_C}$, g_{nC} and $\mathbf{P_C}$·represent the hyperfine tensors, the nuclear g factor and the quadrupole tensor of the nuclear spin $\mathbf{I_C}$ (for $\mathbf{I_C} > 1/2$) of the Coulomb impurity

center, respectively. A_i, P_i and g_{ni} represent the hyperfine tensor, the quadrupole tensor and nuclear g factor of the ligand nucleus i, respectively, for the ^{67}Zn ($I = 5/2$) nuclear spins. Assuming that the hyperfine tensors have nearly axial symmetry one can write the tensor as $A_\parallel = a + 2b$, $A_\perp = a - b$., where a and b are isotropic and anisotropic parts of HF interaction, respectively. For the quadrupole interaction, we can write, in the principal axis system and assuming axial symmetry, $P_{Zn}[I_z^2 - 1/3I(I+1)]$ with $P_{Zn} = 3/2\ P_{zz} = 3q$ and $P_{xx} = P_{yy} = -q$.

To understand these results we consider the isotropic hyperfine interaction a_i which reflects the spin density of the donor electron wave function (Ψ) at the site of the nucleus (r_i)

$$a_i = (8\pi/3)g_e\mu_B g_{ni}\mu_N \left|\psi(r_i)\right|^2, \tag{2}$$

where g_e is the electronic g factor. The related ENDOR transitions have the following frequencies [19]:

$$\nu_{ENDORi} = h^{-1}\left|g_{ni}\mu_B B_0 \pm a_i/2\right|. \tag{3}$$

The Eq. (3) predicts that each nucleus i gives rise to two ENDOR transitions symmetrically placed around its nuclear Larmor frequency $g_{ni}\mu_B B_0/h$ when the quadrupole interaction (QI) is neglected and when $a_i < g_{ni}\mu_B B_0$.

This behavior is indeed observed. The four signals indicated by arrows in Fig. 1c originate in nearby ^{67}Zn nuclei and exhibit an anisotropy. At the bottom of Fig. 1c, 67Zn ENDOR signals measured in three different orientations of the magnetic field relative to the c axis are presented. These signals reveal the quadrupole interaction of the ^{67}Zn nuclear spins ($I = 5/2$, 4.1%), which is superimposed on hyperfine interactions with different Zn shells. The high-frequency part of the ENDOR spectrum with a higher resolution is shown for $B\|c$.

To take into account the quadrupole interaction in the case of axial symmetry the term

$$h^{-1}m_q 3q(3\cos^2\theta - 1), \tag{4}$$

must be added to the equation of ν_{ENDOR} (3) where m_q is the average value of the two nuclear quantum states m_I, $m_{I'}$, between which the nuclear transition takes place. For axial symmetry, one has $q = (eQ_0)/[4I(2I\text{-}1)]V_{ZZ}(r_i)$, where Q_0 is the electric quadrupole moment and $V_{ZZ}(r_i)$ is the electric field gradient. For ^{67}Zn nuclei $I = 5/2$, there are five m_q-values: $m_q = \pm 2, \pm 1$ and 0.

Figure 1d shows the ESE-detected ENDOR transitions of the ^{7}Li nuclear spins as observed in the EPR signal of the shallow donors in Li-doped ZnO quantum dots with a radius of 1.73 nm recorded at 94.9 GHz and $T = 1.8$ K. The two ENDOR transitions are symmetrically placed around the Larmor frequency of ^{7}Li (marked by an arrow). In Fig. 1c and d, the ENDOR transitions of the ^{67}Zn (**c**) and ^{1}H (**d**) nuclear spins are depicted. The ^{67}Zn ENDOR spectrum consists of many unresolved lines placed symmetrically around the ^{67}Zn Larmor frequency (marked by arrow). An absence of the ENDOR signals close to the ^{67}Zn Larmor frequency shows that

remote shells are missing in the QD. The dip in the ENDOR spectrum indicates that for the small QDs, the Zn nuclei at the interface carry a nonzero spin density. This conclusion is in line with the observation that the electronic density at the ZnO/Zn(OH)$_2$ interface, as measured from the line width of the ^{1}H ENDOR signal, increases with decreasing size of the QDs [6].

The ENDOR results show that one can monitor the change of the electronic wave function of a shallow donor in a ZnO semiconductor QDs when entering the regime of quantum confinement by using the nuclear magnetic moment as probes [7, 12]. The model, based on the effective mass approximation [20], that describes the 1 s-like wave function with the Bohr radius of ~1.5 nm for distant shells, does not yield an appropriate description of the electronic wave function when the radius of the QD is reduced below the Bohr radius. The molecular, cluster-type calculations were suggested [9] to be carried out to describe the observed behavior.

Another example of the successful application of high-frequency ENDOR for identifying a shallow donor is the registration of hyperfine and quadrupole interactions of aluminum shallow donors in Al-doped single ZnO crystal and ZnO QDs. Figure 2 shows the W-band ENDOR spectra of 27Al nuclei as observed in the EPR signal of the shallow donor in ZnO:Al single crystal measured in two orientations
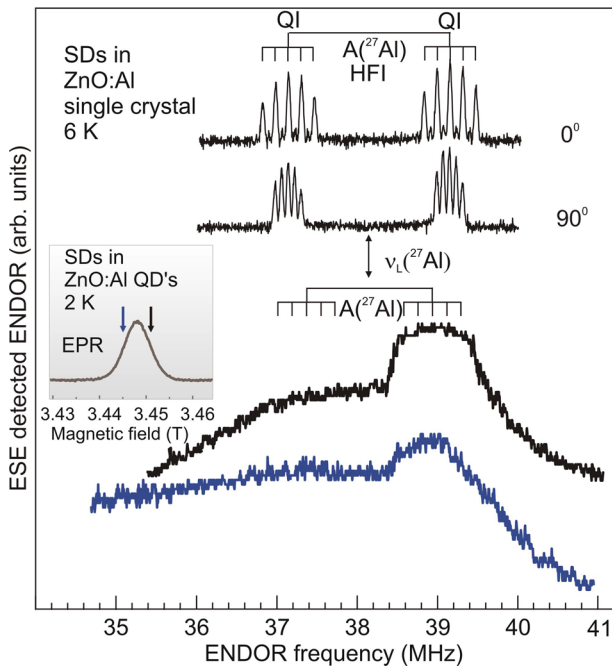
Fig. 2 (Top two spectra) The W-band ESE-detected ENDOR spectra of the [27]Al nuclei in a ZnO:Al single crystal, measured in two orientations of the magnetic field: parallel (0°) and perpendicular (90°) to the c axis. (bottom two spectra) The ESE-detected ENDOR signal of the [27]Al nucleus observed in the EPR signal of the shallow donor in ZnO:Al quantum dots with a radius of about 2.8 nm recorded at 94.9 GHz and $T = 2$ K for two values of the magnetic field within the shallow donor EPR line (inset)

of the magnetic field (top). ENDOR spectra obtained on ZnO:Al QDs with a radius
of about 2.8 nm are presented at the bottom [12, 16, 17]. It is seen that symmetri-
cally around the nuclear Larmor frequency of ^{27}Al ($I=5/2$, abundance 100%) two
groups of ENDOR lines separated by ~ 1.45 MHz are present, which are assigned
to an almost isotropic HF interaction with the ^{27}Al nucleus. The quintet character
of the ENDOR spectrum is expected for ^{27}Al nucleus due to the quadrupole interac-
tion (see Eq. (4)). In QDs, the ENDOR spectrum is a result of averaging HF and QI
interactions in the randomly oriented ZnO nanocrystals. The box-like form of the
ENDOR spectrum is explained by the quadrupole interaction of the ^{27}Al nuclei aver-
aged over all contributions of angles θ followed Eq. (4). Since the EPR spectrum of
the shallow donors is anisotropic, the magnetic field (arrows in the inset) separates
nanocrystals with a specific orientation their c-axes in the magnetic field.

3 Shallow Electron Centers in Ionic-Covalent Silver-Halide Crystals

Silver halides are of particular interest in solid-state physics because their properties
are considered to be of borderline nature between ionic and covalent bonding. Direct
information about the spatial distribution of the wave function of the shallow elec-
tron center (SEC) unpaired electrons was obtained by ENDOR. The electron was
concluded to be mainly contained in a hydrogen-like 1 s orbital with a Bohr radius
of 1.51 nm. The direct reconstruction of the wave function of the intrinsic SEC in
AgCl and AgBr was presented and a model of SEC was suggested in Refs. [21, 22].
The model suggests the electron is shallowly trapped by two adjacent silver ions on
a single cationic site (split-interstitial position), so-called "latent image" in silver
halides.

Figure 3a shows the ESE-detected Ag ENDOR spectra of the shallow electron
centre, $S=1/2$, $g=1.878$, in undoped AgCl crystal recorded with B ‖ [001] orienta-
tion at 94.9 GHz and 1.2 K, under continuous UV irradiation. The ENDOR meas-
ured on the ESE detected single EPR line is shown in the inset (Fig. 3a). An illustra-
tion of Mims ENDOR experiment is presented in the top of Fig. 3a, the microwave
pulse sequence $\pi/2 - \tau - \pi/2 - T—\pi/2$ were applied; typical pulse lengths:

(a) SEC in AgCl — ESE detected EPR, Mims ENDOR RF (NMR), ESE, ν_L (^{107}Ag), ν_L (^{109}Ag), Simulation. ESE detected ENDOR (arb. units) vs ENDOR frequency (MHz).

(b) SEC in AgCl — ν_L (^{37}Cl), ν_L (^{35}Cl), Simulation. ESE detected ENDOR (arb. units) vs ENDOR frequency (MHz).

(c) STE in AgCl $S=1$ — ν_L (^{107}Ag), ν_L (^{109}Ag), Simulation for SEC. ESE detected EPR (arb. units), ESE detected ENDOR (arb. units) vs ENDOR frequency (MHz).
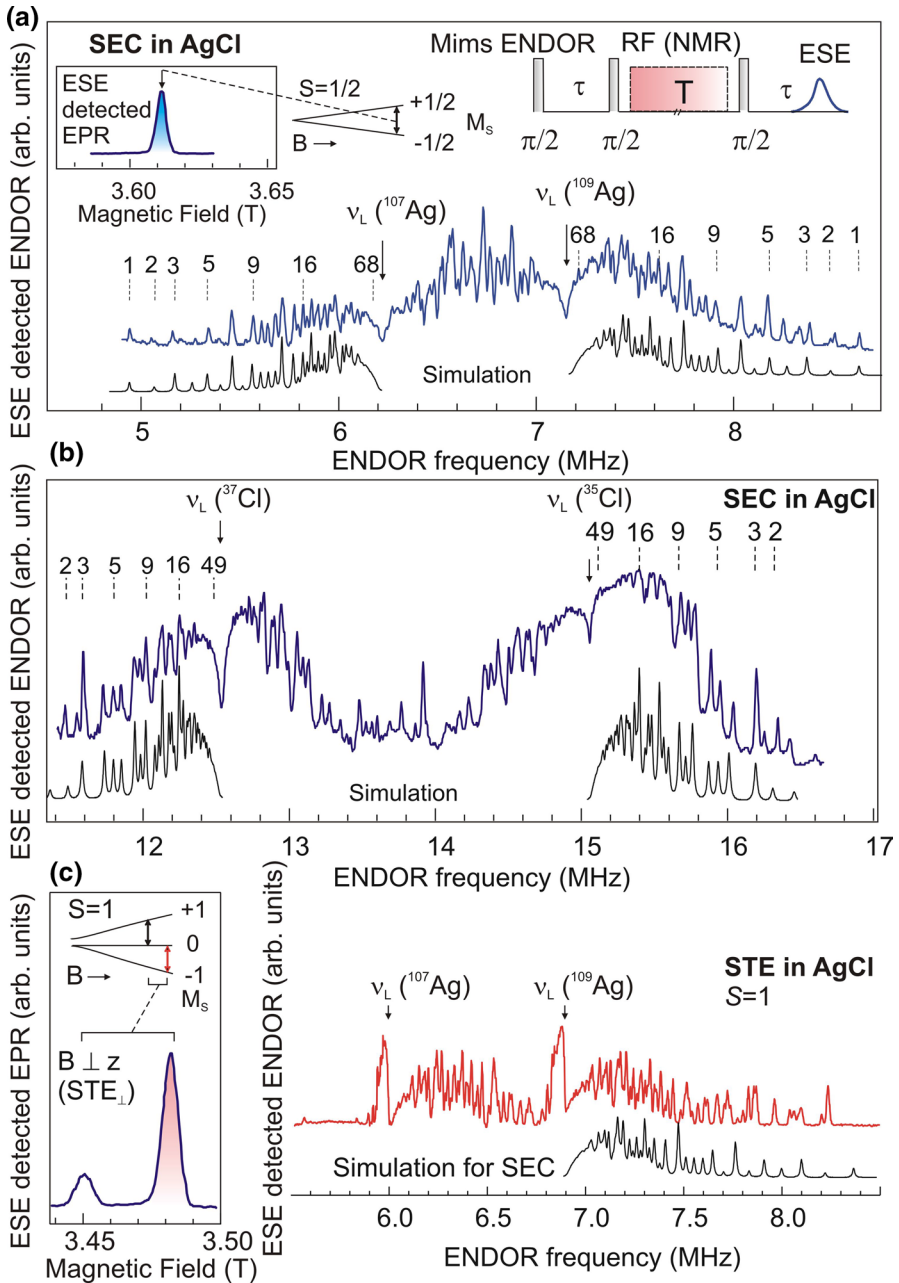
$\pi/2 = 100$ ns, τ between 400 and 900 ns, and the length of RF pulse $= 600$ µs; the repetition rate of the pulse sequence was 33 Hz.

The ENDOR transitions of silver nuclei are shown in Fig. 3a (top spectrum) where the nuclear Larmor frequencies of ^{107}Ag and ^{109}Ag are observable as dips

at 6.224 and 7.156 MHz, respectively. In the case of an electron spin $S = 1/2$ coupled to a single silver nucleus ($I = 1/2$) the ENDOR transitions have the frequencies according to Eqs. (2, 3). Comparison between the recorded (upper curve) and simulated (lower curve) of the ^{107}Ag and ^{109}Ag ENDOR spectrum of the SEC is shown at the bottom of Fig. 3a. Lorentzian line shape was used to simulate the ENDOR spectrum. Figure 3b shows the ESE detected Chlorine ENDOR spectra of the shallow electron centre recorded under the same conditions as in Fig. 3a. The dips at 15.057 MHz and 12.537 in Fig. 3b indicate the nuclear Larmor frequencies of ^{35}Cl ($I = 3/2$, 76%) and ^{37}Cl ($I = 3/2$, 24%), respectively. For a chlorine nucleus ($I = 3/2$) the same expression (1) holds when the quadrupole interaction is neglected. Therefore, Eq. (3) predicts that each nucleus will give rise to two ENDOR transitions symmetrically placed around the corresponding Larmor frequency. The ENDOR spectra proved to be isotropic apart from a few weak lines in the chlorine spectrum which exhibit a quadruple splitting. Comparison between the measured (upper curve) and simulated (lower curve) high-frequency part of the ^{35}Cl and ^{37}Cl ENDOR spectrum of the SEC is shown in Fig. 3b.

An amazing result of the research is the possibility of registering extensive ENDOR signals of self-trapped excitons (STEs) with S = 1 and a lifetime of the order of microseconds [23–27]. In this case, it is possible to study both the strongly delocalized electronic part of the exciton and the localized hole part. That is, it was shown to be possible to "shoe a galloping horse", according to the existing proverb. Self-trapping of charge carriers in a crystal lattice was predicted by Landau in 1933 for electrons [28] but the best-known example is the self-trapped holes (STHs) found in silver halides [29, 30]. In AgCl the self-trapped hole is centred and partly trapped in the cationic sublattice, forming an Ag^{2+} ion inside of a $(AgCl_6)^{4-}$ complex as the result of the Jahn–Teller distortion. The STH in AgCl can capture an electron from the conduction band forming the self-trapped exciton (STE). The properties of the self-trapped excitons, such as exchange coupling, the ordering of the triplet and singlet sublevels, the dynamical properties of the singlet and triplet states, and the hyperfine interaction with the Ag and Cl (Br) nuclei were discussed in Ref. [23–27, 31]. The energy levels diagrams of the triplet self-trapped-excitons in magnetic field B perpendicular (STE$_\perp$) to the distortion z-axis and for SEC are presented in the left panel of Fig. 3c. Ag ENDOR spectra of the triplet state of the STE, recorded at 94.9 GHz and 1.2 K with B along the cubic axis, which is perpendicular to the distortion axis of the STE (STE$_\perp$): the spectrum was obtained by monitoring the high-field EPR transition of STE$_\perp$, which corresponds to a transition between the $M_S = 0$ and $M_S = -1$ sublevels of the triplet.

In Fig. 3c, the ENDOR spectrum of the STE triplet state in AgCl are presented. Two groups of lines can be distinguished both containing transitions originating from ^{107} and ^{109}Ag nuclei. The first group covers a range of a few MHz and is positioned in Fig. 3c above the nuclear Zeeman frequencies of ^{107}Ag and ^{109}Ag. The second group covers a range of only a few tenths of a MHz and is located below the nuclear Zeeman frequencies. The larger part of the ENDOR spectrum is isotropic and has the same form as the SEC spectrum (Fig. 3a), but in some spectral regions an anisotropic behavior was observed. A similarity of the angular dependences for STE with the angular dependences for the STH [30]

was indicated. The ^{35}Cl and ^{37}Cl ENDOR spectra of the STE show essentially the same features as that of silver; however, the interpretation of the chlorine spectra is more complicated owing to the appearance of additional quadrupole lines.

The ENDOR spectrum of the $M_S = 0$ level is compressed by a factor of ∼ 20, as compared to the spectrum of the $M_S = -1$ level. The group of lines covering the broader frequency region in Fig. 3c is thus related to ENDOR transitions in the $M_S = -1$ level, whereas the compressed group corresponds to transitions in the $M_S = 0$ level [25].

The fact that a multitude of lines is present indicates that we are dealing with a delocalized electron that interacts with a large number of Ag and C1 nuclei. For a quantitative analysis of the HF constants, it is necessary to determine the spin density $|\Psi(r_i)|^2$ on each nucleus i. It was shown [32] that, by orthogonalizing a suitable envelope function $\Phi(r)$ to the cores of the lattice ions to allow for the Pauli principle, the spin density on nucleus i may be written as an "amplification factor" K_i, times the density of the envelope function $\Phi(r)$ on that nucleus. Thus $|\Psi(r_i)|^2 = K_i |\Phi(r_i)|^2$. If the envelope function remains approximately constant within each ion core, the value of K_i only depends on the species of ion i and not on its position in the lattice.

Results of the analysis in Refs. [22, 25] is shown in Fig. 4a and b where the densities of the envelope function $|\Phi(r)|^2$ of the SEC (**a**) and STE (**b**) are plotted as a function of (r/d) with the interionic distance $d = 0.2753$ nm. This result is based on the assumption that Φ is centered on the Ag$^+$ lattice position. Open circles and triangles denote the densities derived from the Ag and Cl ENDOR spectra, respectively. It is possible to derive the density of the envelope function on a large number of Ag and C1 shells and some of the Ag shells as indicated in Fig. 4a. It turned out that for shells with a radius larger than about 1.2 nm, the derived electron densities indeed obey the expected exponential form with a Bohr radius $r_0 = 1.66$ nm for SEC and $r_0 = 1.51$ nm for STE (dashed line in Fig. 4a, b), however, for nearby shells, there is a clear deviation. This results from the neglect of the influence of the chemical nature of the binding centre and it illustrates the need for the so-called central cell correction in the effective mass theory [20]. The derived densities can be very well described by the following normalized monotonically decreasing function [1]

$$|\Phi(r_i)|^2 = = (7\pi r_1)^{-1}(1 + r/r_1)^2 \exp(-2r/r_1), \tag{5}$$

which for comparison is plotted as a solid line in Fig. 4a, b using amplification factors $K_{Ag} = 2450$, $K_{Cl} = 1060$ and $r_1 = 0.994$ nm.

Figure 3 shows a good overall agreement between the recorded and the simulated spectrum. The simulation, however, does not account for all features observed at frequencies above 8.1 MHz. The ENDOR lines in this region correspond to shells that lie close to the centre of Φ and suggest the presence of the lattice distortion in the direct surrounding of the binding core. One can see that even the contribution of the 68th silver shell can be resolved. Figure 3b, bottom, compares the recorded spectrum of the ^{37}C1 ENDOR to its simulation, a good overall agreement is seen and the contributions up to the 49th chlorine shell can be observed. The results were
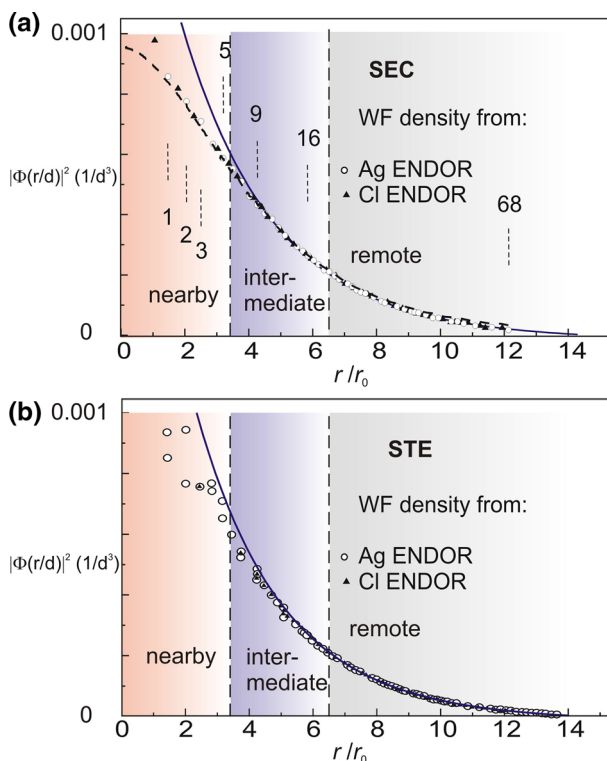
Fig. 4 Density of the envelope function $|\Phi(r)|^2$ of the SEC (**a**) and STE (**b**) as a function of (r/d) with the interionic distance $d=0.2753$ nm. Open circles and triangles denote the densities derived from the Ag and Cl ENDOR spectra, respectively. Some neighboring silver shells are indicated. Solid lines illustrate the exponential radial dependence in the remote region corresponding to a Bohr radius $r_0=1.66$ nm for SEC and $r_0=1.51$ nm for STE

obtained by placing the centre of the envelope function Φ on the Ag^+ lattice position and this turned out to be the only position for which one could obtain a satisfactory analysis of the Ag and Cl ENDOR spectra.

Information concerning the charge of the intrinsic SEC can be obtained from ENDOR on the STE. The STE consists of an electron loosely bound to a STH and can therefore be considered as a special case of an SEC. It is possible to derive the spatial distribution of the electronic part of the STE, in a similar way as described here for the intrinsic SEC. The density of Φ for the STE is plotted as a function of r in Fig. 4b. One can found that the shallowly trapped electron of the STE also behaves almost like a hydrogen 1 s electron, centered on the Ag^+ lattice position, with a Bohr radius $r_0=1.51$ nm [25]. The close agreement of this value with the one derived for the intrinsic SEC ($r_0=1.66$ nm) [22] and the fact that the electron of the STE is shallowly bound by the Coulombic field of an STH indicates that the SEC has the same Coulombic charge. For SEC in AgBr, $r_0=2.48$ nm [22].

Since these results show that the intrinsic SEC is located on the Ag^+ lattice position, the previously suggested model of an interstitial Ag^0 "atom", which consists of an electron loosely bound to a single interstitial Ag^+ ion, was rejected. Such molecular Ag_2^+ ions have been observed in KC1 crystals doped with silver after X-ray irradiation at room temperature, however, in KC1 they form, in contrast to the present situation, deep electron traps [33].

In conclusion, the presented ENDOR results prove that the $g = 1.878$ paramagnetic centre in undoped AgCl originates from an SEC. It is shown that the centre is located on the Ag lattice position [35], the centre is concluded to be of intrinsic origin. The electron is suggested to be shallowly trapped in the Coulombic field of two adjacent Ag^+ ions symmetrically placed on a single cationic site—the split-interstitial position [21, 22, 34, 35].

4 Dynamic Nuclear Polarization in Crystal Lattice by Saturation of EPR Transitions on Shallow-Level Donors in ZnO and AgCl

Dynamic nuclear polarization (DNP) in condensed systems has been widely developed and used to increase the efficiency of nuclear magnetic resonance (NMR) [13, 15, 36–38]. DNP effects, realized by saturation of EPR transitions on shallow-level carriers in semiconductors and their nanostructures, have been in the spotlight since their first discovery by Overhauser [36]. In this case, the nuclear polarization can be significantly increased due to the isotropic hyperfine interaction between the magnetic moments of electrons and nuclei, which is described by a part of the Hamiltonian $aS{\cdot}I$ in the form of the operator expression $1/a(S_+I_- + S_- I_+)$. The operator S_+ flips the projection of the electron spin upward, while the operator I_- simultaneously flips the projection of the magnetic moment of the nucleus in the opposite direction, that is, as a result, the angular momentum is conserved. The second term does the same thing, only in opposite directions. Saturation of the EPR line of shallow donors causes DNP as a result of "flip-flop" relaxation of electron and nuclear spins, the so-called Overhauser effect [36].

The enhancement of nuclear polarization in the ideal case has the form $f = [1 + (g_e\mu_B)/(g_n\mu_N)]$. Here g_e and g_n are electronic and nuclear g factors, respectively; μ_B and μ_N Bohr magneton and nuclear magneton, respectively. That is, as a result of DNP, the difference between the populations of nuclear spin levels becomes close to that for electron spin levels; ideally, the polarization of nuclei can be increased by three orders of magnitude. The Boltzmann distribution plays a key role in achieving a high DNP. Thus, it becomes obvious that it is necessary to use low temperatures and strong magnetic fields (high operating frequency of the EPR spectrometer).

We will consider DNP processes in crystals of the II-VI type (using ZnO as an example) and I-VII (AgCl), where we previously found shallow donors with a Bohr radius of about 1.5 nm. Our data on electron-nuclear double resonance showed that the wave function of shallow donors in these crystals covers dozens of coordination spheres. In this case, in all coordination spheres there are nuclei with magnetic moments and there is a nonzero density of wave functions on these nuclei, that is,

there is an isotropic hyperfine interaction with the constants a_i. Natural zinc has only one isotope [67]Zn with a nuclear magnetic moment, the natural content is 4.1%, the nuclear spin is $I = 5/2$, and the nuclear g-factor $g_n = 0.3503$. Oxygen has one isotope with a nuclear magnetic moment, but its concentration is negligible, so we will not consider it. In AgCl, a different situation is realized, all isotopes of silver and chlorine have nuclear magnetic moments, moreover, the nuclear g-factors of silver isotopes on the one hand and chlorine isotopes on the other have opposite signs, which creates a unique situation for studying DNP effects. Isotopes [107]Ag and [109]Ag have the same nuclear spins $I = 1/2$, natural abundance 51.83%, nuclear g-factor $g_n = -0.2272$ for [107]Ag and 48.17% and $g_n = -0.2617$ for [109]Ag; for isotopes [35]Cl and [37]Cl, nuclear spins $I = 3/2$, [35]Cl content 51.83%, $g_n = 0.5479$; the [37]Cl content is 48.17% and $g_n = 0.4561$. It can be seen that the nuclear g-factors for the Ag and Cl isotopes have different signs, therefore, the sign for Cl is similar to the sign for the nuclear g-factor of the [67]Zn isotope ($I = 5/2$, 4.1%, $g_n = 0.3503$). Consequently, the DNP of Cl nuclei leads to a shift of the EPR line in the direction of decreasing the magnetic field, similar to the shift caused by the DNP of [67]Zn nuclei. On the contrary, DNP of Ag nuclei will lead to a shift in the direction of increasing magnetic field. Naturally, Ag and Cl nuclei have different relaxation characteristics and different hyperfine interactions with an unpaired shallow donor electron [36]. As a result, a splitting of the EPR lines was observed for shallow donors in AgCl, which is apparently caused by the difference in the DNP effect for different groups of shallow donors inside the AgCl crystal.

Figure 5a shows the shifts of the EPR lines in a ZnO crystal due to the DNP effect for [67]Zn nuclei as a result of preliminary pulsed saturation of shallow donors with a resonant microwave field at a frequency of 275 GHz at different temperatures. Subsequent EPR signals, located below, were recorded after preliminary resonant microwave irradiation for 2 min in the region of the lines indicated by the arrows. The DNP effect depends on temperature and at temperatures above 10 K, DNP is not observed.

In Fig. 5b, an influence of preliminary continuous resonant microwave irradiation on the position of the ESE detected EPR lines of shallow donors in an AgCl single crystal at 94.9 GHz and 1.6 K is demonstrated. The EPR signal at the top is an unperturbed line. Subsequent EPR signals, located below, were recorded after preliminary continuous resonant microwave irradiation for 2 min in the region of the lines indicated by the arrows. For comparison, Fig. 5c shows the shifts of the EPR lines in a magnetic field due to the DNP effect as a result of preliminary resonant microwave CW irradiation of the ZnO crystal; the same scale of magnetic fields was used. It is seen that the shifts in the ZnO crystal are significantly less than the corresponding shifts in the AgCl crystal, which is due to the low content of the [67]Zn isotope in the natural crystal.

The possibility of obtaining direct information about the spatial distribution of the wave function of unpaired electrons based on ENDOR studies is particularly attractive because it allows for quantitative measurement of the effect of confinement on the shape and properties of the wave function in quantum dots. Figure 6a shows the shift of the hole and antihole in the EPR transition of the shallow Li donor in ZnO QDs with a radius of 1.6 nm induced by CW microwave irradiation
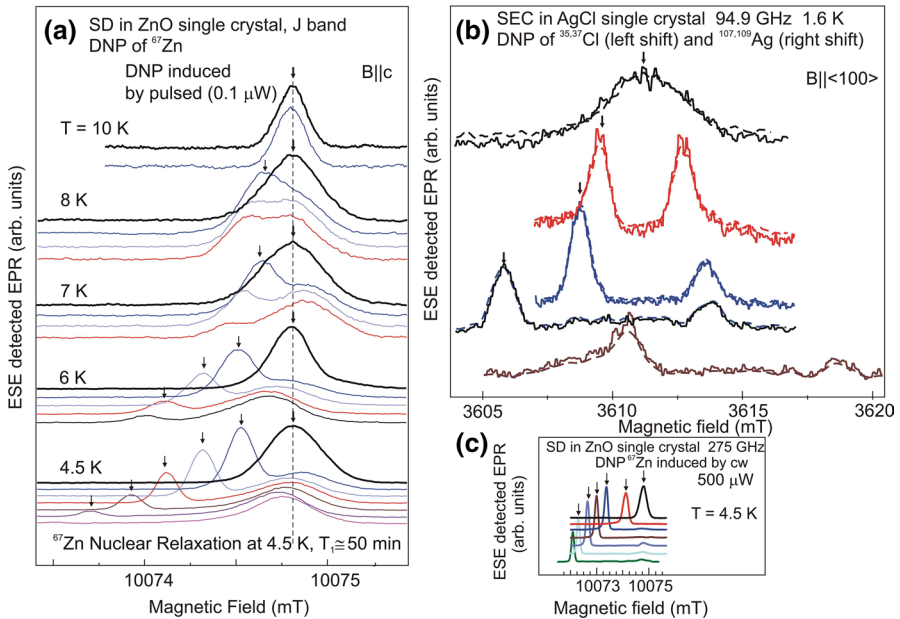
Fig. 5 a Shifts of the EPR lines in a ZnO crystal due to the DNP effect for ^{67}Zn nuclei as a result of preliminary pulsed saturation of shallow donors with a resonant microwave field at a frequency of 275 GHz. Temperature dependence of the DNP effect for ^{67}Zn nuclei in a ZnO crystal. **b** Influence of preliminary continuous resonant microwave irradiation on the position of the ESE detected EPR lines of shallow donors in an AgCl single crystal at a frequency of 94.9 GHz and a temperature of 1.6 K. The EPR signal at the top is an unperturbed line. Subsequent EPR signals, located below, were recorded after preliminary continuous resonant microwave irradiation for 2 min in the region of the lines indicated by the arrows. **c** For comparison, the shifts of the EPR lines in a magnetic field due to the DNP effect as a result of preliminary resonant microwave continuous wave (CW) irradiation in the ZnO crystal are shown; the same scale of magnetic fields was used. It is seen that the shifts in the ZnO crystal are significantly less than the corresponding shifts in the AgCl crystal, which is due to the low content of the ^{67}Zn isotope in the natural crystal
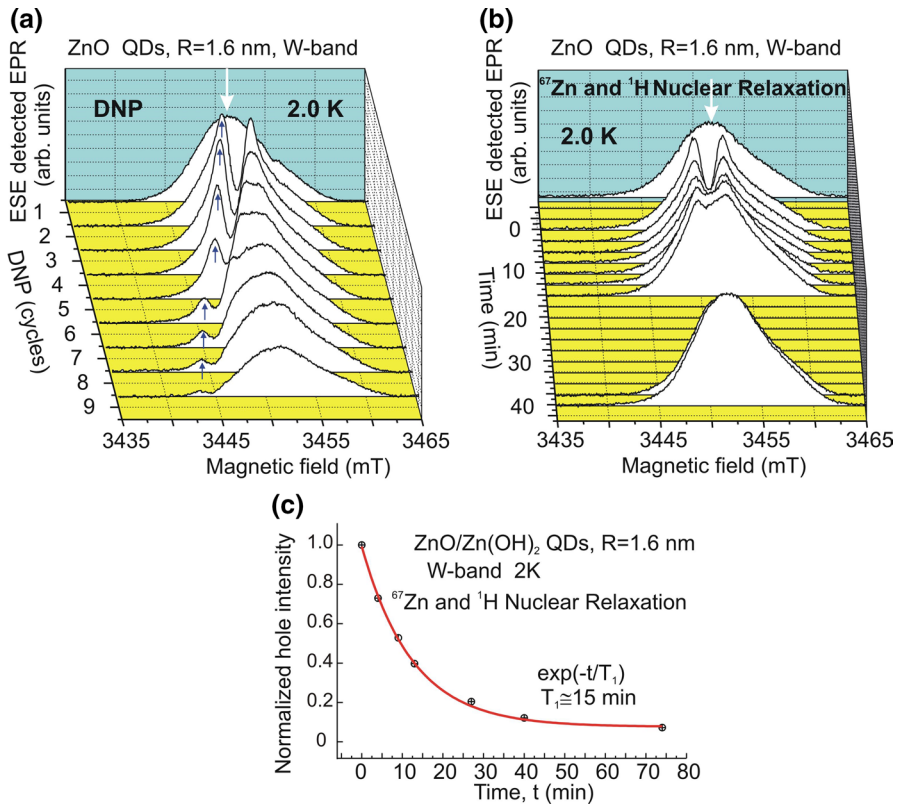
at 94.9 GHz at 2 K. In the upper curve the EPR line is recorded without preirradiation. The second recording from the top is obtained after CW microwave irradiation for 3 min at the center of the unperturbed line. The next curves are observed after CW microwave irradiation for 3 min at the maximum of the antihole of the previous recording. Finally, the antihole stabilizes at a position shifted by about 5 mT with respect to the original position, which caused by the maximum polarization of ^{67}Zn nuclei in the core and ^{1}H nuclei in the shell (core/shell QD structure).

Figure 6b demonstrates the relaxation of the nuclear polarization in the EPR signal of the shallow donor in ZnO nanocrystals with a radius of 1.6 nm as monitored by the evolution of the hole burnt in the EPR line by 3 min CW microwave irradiation at 94.9 GHz. In the upper curve, the EPR line is recorded without pre-irradiation. The second recording from the top is obtained after the CW microwave irradiation. It is seen that slowly the hole and antihole decrease and that the EPR spectrum recovers to its initial unperturbed form.

(a) ZnO QDs, R=1.6 nm, W-band
ESE detected EPR (arb. units)
DNP   2.0 K
DNP (cycles)
1 2 3 4 5 6 7 8 9
Magnetic field (mT)
3435 3445 3455 3465

(b) ZnO QDs, R=1.6 nm, W-band
ESE detected EPR (arb. units)
^{67}Zn and ^{1}H Nuclear Relaxation
2.0 K
Time (min)
0 10 20 30 40
Magnetic field (mT)
3435 3445 3455 3465

(c)
Normalized hole intensity
1.0 0.8 0.6 0.4 0.2 0
ZnO/Zn(OH)$_2$ QDs, R=1.6 nm
W-band 2K
^{67}Zn and ^{1}H Nuclear Relaxation
$\exp(-t/T_1)$
$T_1 \cong 15$ min
Time, t (min)
0 10 20 30 40 50 60 70 80

Fig. 6 **a** The shift of the hole and antihole in the EPR transition of the shallow Li donor in ZnO QDs with a radius of 1.6 nm induced by CW microwave irradiation at 94.9 GHz at 2 K. In the upper curve the EPR line is recorded without preirradiation. The second recording from the top is obtained after CW microwave irradiation for 3 min at the center of the unperturbed line. The next curves are observed after CW microwave irradiation for 3 min at the maximum of the antihole of the previous recording. Finally, the antihole stabilizes at a position shifted by about 5 mT with respect to the original position. **b** The relaxation of the nuclear polarization in the EPR signal of the shallow donor in ZnO nanocrystals with a radius of 1.6 nm as monitored by the evolution of the hole burnt in the EPR line by 3 min cw microwave irradiation (20 mW) at 94.9 GHz at 2 K. In the upper curve, the EPR line is recorded without preirradiation. The second recording from the top is obtained after the cw microwave irradiation. It is seen that slowly the hole and antihole decrease and that the EPR spectrum recovers to its initial unperturbed form. **c** Decrease hole burnt in the EPR line in Fig. 9b after switching off the resonant microwave pumping, which caused the maximum polarization of ^{67}Zn nuclei in the core and ^{1}H nuclei in the shell (core/shell QD structure), due to relaxation of ^{67}Zn and ^{1}H nuclei with time $T_1 \approx 15$ min

In Fig. 6c, a decrease hole burnt in the EPR line in Fig. 6b after switching off the resonant microwave pumping due to relaxation of ^{67}Zn and ^{1}H nuclei with the spin–lattice relaxation time T_1 of about 15 min is demonstrated. More sophisticated experiments can make it possible to probe nuclear relaxation for nuclei located at different distances from a shallow donor.

Thus, it was demonstrated that dynamic nuclear polarization of nuclear spins can be achieved in ZnO and AgCl by saturating the EPR transition of a shallow donor

present in these crystals (and based QDs) using high-frequency radiation at low temperatures corresponding to a high Boltzmann factor. An increase in nuclear polarization opens up the possibility of studying semiconductor nanostructures by NMR methods, which was previously impossible due to the low sensitivity of traditional NMR methods.

5 Shallow Donors in AlN Crystal

Aluminum nitride (AlN) is a direct-bandgap semiconductor with an energy gap of about 6.0 eV. AlN has considerable potential for optoelectronic devices operating in the ultraviolet (UV) spectral region [39]. Nominally undoped AlN crystals have the n-type conductivity and high resistance due to the presence of deep-level defects. The n-type conductivity of semiconductors can be affected by a transition of the shallow donors to a deep state. Experimental and theoretical studies of semiconductor's electronic properties have demonstrated that the shallow donor could give rise to the two types of electronic states, either a shallow state with a delocalized effective-mass-like wavefunction or a deep state with a localized wavefunction. The latter (usually called the DX center) arises due to the lattice distortions at or near the donor site and exhibits a negative correlation energy U for the electrons trapped at this site [40–42].

High-frequency EPR and ENDOR were demonstrated to be the methods of choice for the identification of the effective-mass-like shallow donors in semiconductors (see Sects. 2 and 3) [17, 43]. In this paper, we report the results of EPR and ENDOR on as-grown bulk AlN crystals that prove the presence of shallow donors with a strongly delocalized wavefunction. The search of the SDs with a stable state at room temperature is one of the major challenges in materials based on AlN. An important applied problem is to find the impurity, which provide a reliable n-type conductivity at room temperature not affected by the DX-relaxation.

Figure 7a and b show the ESE-detected ^{27}Al ENDOR signal of the shallow donor in the as-grown undoped AlN single crystal at 1.8 K after cooling down from room temperature in the dark (black line) and after 10 min light illumination (red line): ^{27}Al ENDOR signals measured in orientation $\theta = 90°$, $B \perp c$ (**a**) and ^{27}Al ENDOR signals measured in orientation $\theta = 54°$ (**b**). The ENDOR was measured on the ESE detected non-resolved single EPR line of SDs, shown in the inset of Fig. 7a. The observed SD EPR signal is characterized by a slightly anisotropic g factor of $g_{\parallel} = 1.9900$ and $g_{\perp} = 1.9894$ due to the hexagonal symmetry of the AlN crystal. It is useful to compare g-factors for SDs in AlN and ZnO ($g_{\parallel} = 1.9569$ and $g_{\perp} = 1.9552$), which support the assignment of the indicated resonances to SD's.

After cooling in the dark, only a weak SD EPR signal is observed. After illumination with light with a wavelength shorter than 700 nm, a strong SD EPR signal appears. This EPR signal, once excited at a low temperature, remains at a low temperature after the light is turned off. The light-induced SD EPR signal disappears after heating above 200 K.

As mentioned above, for $S = 1/2$, the HF interaction constant A_i for each ^{27}Al i-nucleus causes two ENDOR transitions symmetrically located around its nuclear
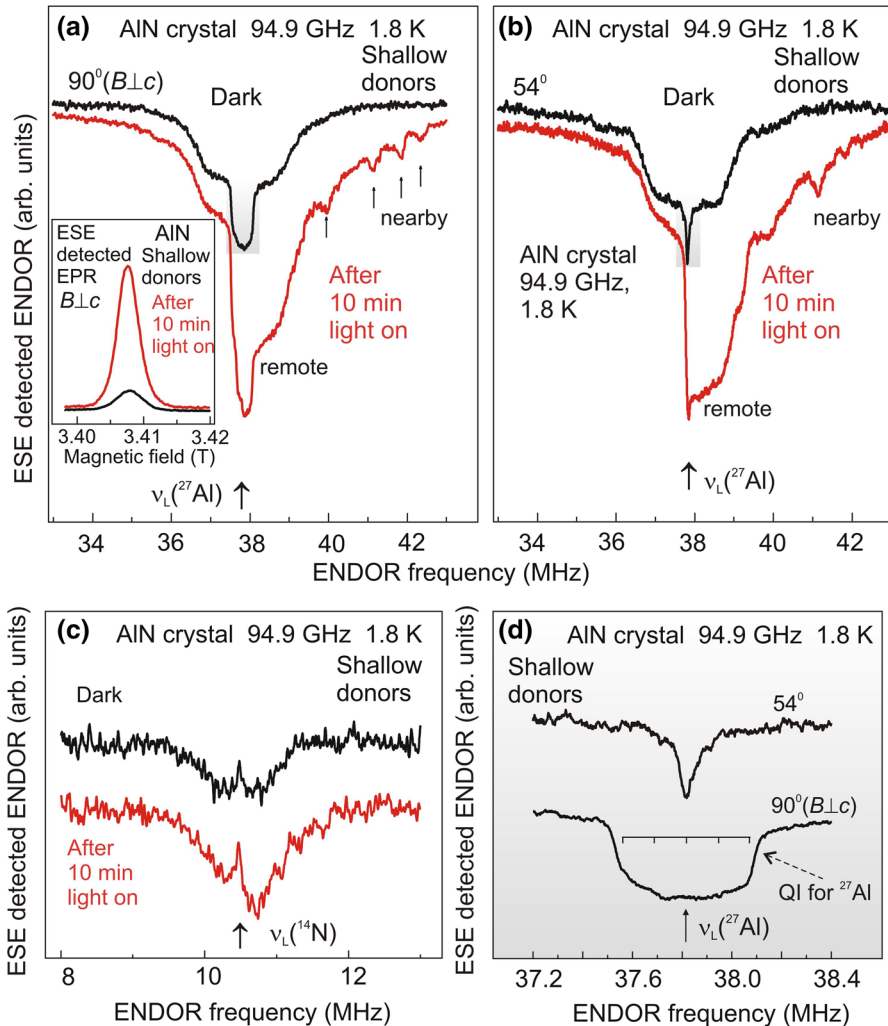
Fig. 7 a, **b** The ESE-detected 27Al ENDOR signal of the SD in as-grown undoped AlN single crystal measured at $T = 1.8$ K with (red line) and without (black line) optical excitation; **a** [27]Al ENDOR signals measured in orientation $\theta = 90°$, $B \perp c$, (inset) ESE-detected EPR spectra of SD at 94.9 GHz at 1.8 K in the orientation $B \perp c$ after cooling down from room temperature to 1.8 K in the dark (black line) and after 10 min light illumination (red line). **b** [27]Al ENDOR signals measured in orientation $\theta = 54°$. **c** [14]N ENDOR signals measured in orientation $\theta = 90°$ after cooling down from room temperature to 1.8 K in the dark (black line) and after 10 min light illumination (red line). **d** the central part of the SD ENDOR signal of ^{27}Al nuclei measured after cooling down from room temperature to 1.8 K in the dark in two orientations: $\theta = 54°$ and $\theta = 90°$ which reveals the quadrupole interaction

Larmor frequency (quadrupole interaction is neglected). This symmetrical behavior is indeed observed for the "dark" SD signal, although the HF lines are not resolved, as is the case with SD in ZnO or AgCl (see Sects. 2 and 3, respectively). In contrast, a significant difference in intensity is observed for the light-induced SD ENDOR

signals, which are located in Fig. 7a and b above the nuclear Larmor frequency ^{27}Al and below this frequency. This difference in intensity is highly temperature-dependent and increases with decreasing temperature. The ENDOR spectra consist of many lines that appear to be isotropic, with the exception of a few lines in the Al spectrum, which show a slight orientation dependence of the linewidth and which are shown by arrows in Fig. 7a.

The light-induced SD ENDOR spectrum shown in Fig. 7a and b can be understood if we assume that we are dealing with a triplet ground state of two exchange-coupled SD spins. More intense signals above the nuclear Larmor frequency of ^{27}Al are associated with ENDOR transitions at the lower $M_S = -1$ sublevel, while less intense signals below the nuclear Larmor frequency correspond to a transition at the $M_S = +1$ since significant difference in populations of triplet sublevels at such a low temperature and large Zeeman splitting is expected. Taking in account this observation together with the fact that the nuclear g-factor for ^{27}Al has a positive sign, we conclude that the HF interaction A_i has a positive sign, i.e., SD induces a positive spin density of electrons on Al nuclei. A similar temperature-dependent asymmetry is expected for ^{14}N nuclear spins. This effect is indeed observed in ^{14}N ENDOR spectrum presented in Fig. 6c.

In Fig. 7c, the central part of the SD ENDOR signal of ^{27}Al nuclei (highlighted in gray in Fig. 7a and b) is presented which was measured after cooling down from room temperature to 1.8 K in the dark in two orientations: $\theta = 54°$ and $\theta = 90°$. This pattern shows the quadrupole interaction (QI) with ^{27}Al nuclei ($I = 5/2$).

As observed in Fig. 7a and b, the strong intensity of the ENDOR line at the Larmor frequency of ^{27}Al is caused by the superposition of a large number of ENDOR lines with very small HF interaction. This confirms the assumption that the donor wave function is significantly delocalized in the crystal. The effective Bohr radius of the 1 s-like envelope of the wave function, calculated taking into account the effective electron mass and the dielectric constant of AlN, is 1.5 nm. That is, the value of the Bohr radius of shallow donors in AlN is approximately the same as in ZnO and AgCl (see Sects. 2 and 3).

Optically excited pairs of SD's with a strong isotropic exchange interaction J can be described in terms of the corresponding singlet ($S=0$) and triplet ($S=1$) states separated J. To find J, the spin–lattice relaxation rate was measured as a function of temperature. The results are shown in Fig. 8a, where the temperature dependence of spin–lattice relaxation rate $1/T_1$ for ESE detected EPR spectra of shallow donors in AlN single crystal measured at 94.9 GHz after cooling down in the dark (filled black circles) and after 10 min light illumination (open red circles). The dashed and bold lines are a fit of the temperature dependences of spin–lattice relaxation time T_1 for dark and light-induced ESE signals, respectively.

For the dark signal, the $1/T_1$ is independent of temperature. For light-induced signal $1/T_1$ is in part due to the Orbach process [44], that is, thermally induced excitation and decay from a singlet state that is 24 about cm^{-1} higher than the lowest triplet state is taken place. The energy of exchange interaction increases exponentially with decreasing distance between isolated donors. For a J value of 24 cm^{-1}, the distance between bound donors was found to be ~ 5.5 nm.
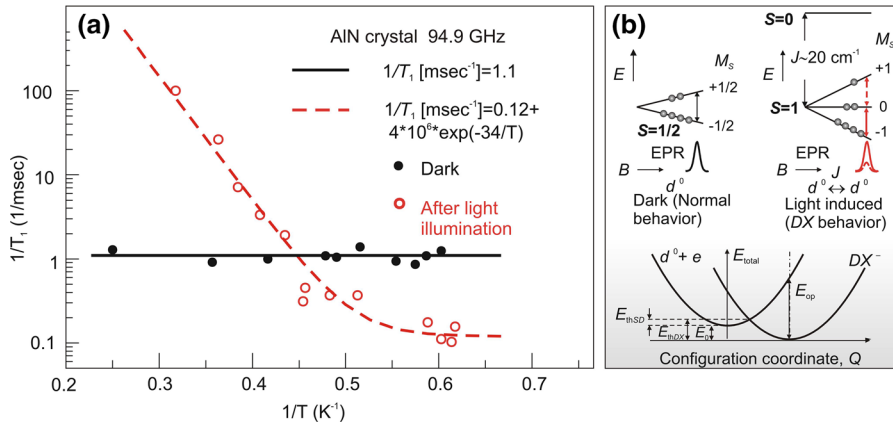
Fig. 8 **a** The temperature dependence of spin–lattice relaxation time T_1 of SDs in AlN single crystal measured without optical excitation (filled black circles) and after 10 min light illumination of the sample (open red circles). The dashed and bold lines are fits of the T_1 temperature dependences. **b** (top) Energy levels diagrams for normal shallow donors in AlN measured after cooling down in the dark ($S=1/2$) and the light-induced shallow donor pairs coupled by exchange interaction $J \approx 20$ cm^{-1} with DX behavior. A schematic diagram of the positions of the singlet and triplet states of the shallow donor pair as a function of the magnetic field is presented. The solid arrow and solid EPR line indicate the observed transition and the signal for the lowest populated energy levels $M_S = -1 \leftrightarrow M_S = 0$, the broken arrow and the broken EPR line represent the transition and the signal for upper less populated levels $M_S = 0 \leftrightarrow M_S = +1$. The Boltzmann distribution of the populations of the levels is symbolically indicated by different numbers of filled circles. (bottom) Configuration-coordinate diagram for DX$^-$ centers and shallow donor pairs d° coupled by the exchange interaction in AlN

In the top of Fig. 8b, the energy levels diagrams for normal shallow donors in AlN measured after cooling down in the dark ($S=1/2$) and the light-induced shallow donor pairs coupled by exchange interaction $J \approx 20$ cm^{-1} with DX behavior are presented. A schematic diagram of the positions of the singlet and triplet states of the shallow donor pair as a function of the magnetic field is depicted. The solid arrow and solid EPR line indicate the observed transition and the signal for the lowest populated energy levels $M_S = -1 \leftrightarrow M_S = 0$, the broken arrow and the broken EPR line represent the transition and the signal for upper less populated levels $M_S = 0 \leftrightarrow M_S = +1$. The Boltzmann distribution of the populations of the levels is symbolically indicated by different numbers of filled circles. It is not possible to resolve the two transitions (solid and dashed arrows) in EPR, but they can be easily separated in the high-frequency ENDOR spectra! A configuration-coordinate diagram for DX$^-$ centers and shallow donor pairs d$^\circ$ coupled by the exchange interaction in AlN is shown at the bottom of Fig. 8b. These SD pairs are believed to show a negative correlation energy U.

The microscopic nature of the shallow donor could be identified if the HF interaction of the central nucleus could be determined experimentally. In the present experiments, a search for Si, C or O was unsuccessful, probably due to the low natural abundance of the isotopes with nuclear magnetic moments. The character of the HF interaction with Al shells is different for dark and light-induced shallow donors, which could give information about the position of the shallow donor in

cationic (Al) or anionic (N) sublattice. The larger gyromagnetic ratio and spin of [27]Al nucleus indicate that the HF interaction with the Al nuclei should dominate and the contribution to the linewidth of the N nuclei may be neglected. The strong HF interaction for light-induced SD support the assignment to the impurity in anionic sublattice (e.g. oxygen in N position). At the same time, a shallow donor with normal behavior can belong to Si or C in the Al position.

6 Electronic Structure of Shallow Donors and Shallow Acceptors in Silicon Carbide

Silicon Carbide (SiC) is a wide-band-gap semiconductor for applications in high-frequency, high-temperature and high-power electronic devices. For this purpose n- and p-type SiC is grown by incorporation of donor impurities, like N, or acceptor impurities, like B, Al and Ga. For the development of SiC-based semiconductor devices, a deep understanding of the electronic and structural properties of the donor and acceptor centers is imperative. SiC also possesses such a unique property as polytypism, i.e., the ability to form many different crystal structures (cubic, hexagonal or rhombic). Up to date around 250 different polytypes of SiC are known. This property serves as a complicating factor since SiC exhibits significantly different band structure depending on its polytype, additionally, the donor and acceptor impurities can occupy different crystallographic sites in the SiC polytypes.

An important issue is the spatial delocalization of the electronic wave function of the donor and acceptor centers in semiconductors. In the ENDOR experiments, the hyperfine interaction between the unpaired electron spin of the donor or acceptor and the nuclear spin of the surrounding atoms is determined, which is then translated into the spin density of the electronic wave function at the various atomic positions.

6.1 Shallow Donors in SiC

In this section, the results of the high-frequency ENDOR study of the N shallow donor in the two main SiC polytypes, 4H-SiC and 6H-SiC, will be presented. High-frequency EPR measurements at 142 GHz [45] allowed to separate overlapping EPR lines, owing to the high spectral resolution, and to assign the various EPR lines to specific sites in the SiC lattice, X-band ENDOR measurements were reported in [46]. High-frequency ENDOR study of N shallow donors in SiC was reported in [47]. An important advantage of the ENDOR study [47] is that it was conducted at a microwave frequency of 95 GHz, that is, ten times higher than the standard frequency at which previous measurements were performed. The high spectral resolution not only made it possible to distinguish between different positions of nitrogen in the EPR spectra but also led to the separation of the ENDOR signal from [13]C (natural abundance 1.11%, $I = 1/2$) and [29]Si (natural abundance 4.67%, $I = 1/2$). Thus, the HF interaction of the unpaired electron spin with the surrounding nuclear spins can be determined in great detail, providing information from which the spatial delocalization of the electron wave function can be derived.
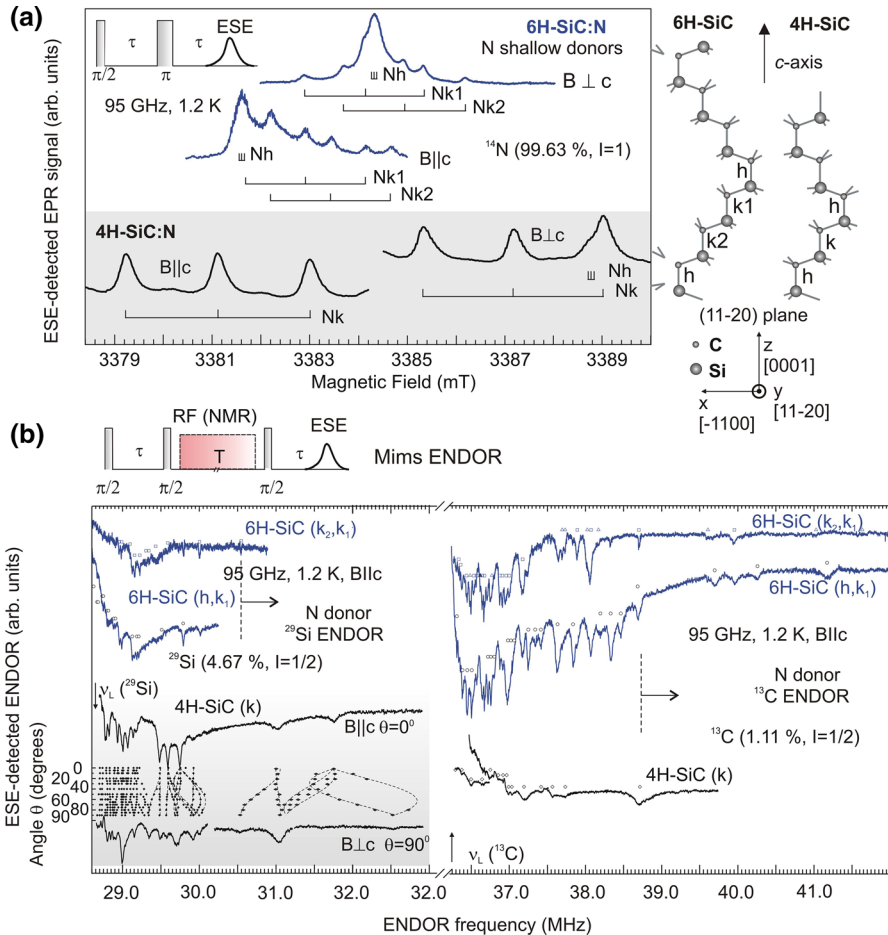
Fig. 9 **a** The ESE-detected EPR spectra of the N shallow donors in 4H-SiC and 6H-SiC single crystals measured at 1.2 K and 95 GHz for two different orientations of the magnetic field, $B\|c$ and $B\perp c$. The three EPR hyperfine lines corresponding to the nitrogen donor in cubic-like sites are indicated by Nk in 4H-SiC; Nk1 and Nk2 in 6H-SiC. (right panel) A schematic representation of the 4H-SiC and 6H-SiC crystal structure. The SiC crystal is built up of tetrahedrons, with four bonds for every atom. Two of the bonds lie in the (11–20) plane of the figure and parallel to the direction of the c-axis a staircase pattern is formed. For 6H-SiC this pattern gives rise to three non-equivalent sites, k1, k2 and h, for 4H-SiC there are two sites, k and h. **b** The ESE-detected ^{29}Si and ^{13}C ENDOR spectra on the right side of the Larmor frequencies in 4H-SiC and 6H-SiC for $B\|c$. The upper spectrum belongs to the N donor substituting carbon atom in the k2 site in 6H-SiC. The positions of the corresponding lines are marked by diamonds. The middle spectrum corresponds to the N donor occupying k1 position. The lower spectrum belongs to the N donor in k site in 4H-SiC. The ^{29}Si k1, k2 site lines are both marked by squares, the positions of the h site lines are marked by circles. The ^{13}C positions of the h site lines are marked by open circles, those of the k1 site lines by squares and those of the k2 site by triangles. The ^{29}Si and ^{13}C nuclear Larmor frequencies are indicated by arrows. The orientational dependence of the ^{29}Si ENDOR lines of the k site in 4H-SiC in the (11–20) or (xz) plane. The spectra have been corrected for the shift of the nuclear Larmor frequency with respect to the orientation $B\|c$

Figure 9a shows the ESE-detected EPR spectra of the nitrogen shallow donors in 4H-SiC and 6H-SiC single crystals as measured at 95 GHz and 1.2 K for two different extreme orientations of the magnetic field in the crystal, $B \| c$ and $B \perp c$. In Fig. 9a, three EPR hyperfine lines connected to the quasi-cubic sites are observed, indicated by Nk in 4H-SiC; Nk1 and Nk2 in 6H-SiC. The HF splitting of the h site EPR line is too small to be resolved in EPR. A schematic representation of the 4H-SiC and 6H-SiC crystal structure is presented in the right panel. The SiC crystal is built up of tetrahedrons, with four bonds for every atom. Two of the bonds lie in the (11–20) plane of the figure and parallel to the direction of the c-axis a staircase pattern is formed. For 6H-SiC this pattern gives rise to three non-equivalent sites, cubic-like k1, k2 and hexagonal h, for 4H-SiC there are two sites, k and h.

The EPR and ENDOR data for the N donors in SiC can be described by a spin Hamiltonian of the following form (see also Eq. 1):

$$\hat{H} = \mu_B \mathbf{S} \cdot \mathbf{g} \cdot \mathbf{B} + \mathbf{S} \cdot \mathbf{A}_N \cdot \mathbf{I}_N - g_{nN}\mu_N \mathbf{I}_N \cdot \mathbf{B} + \mathbf{I}_N \cdot \mathbf{P}_N \cdot \mathbf{I}_N - \Sigma(\mathbf{S} \cdot \mathbf{A}_i \cdot \mathbf{I}_i - g_{ni}\mu_N \mathbf{I}_i \cdot \mathbf{B}). \quad (6)$$

Here $S = 1/2$, $\mathbf{g}$ is the electronic g tensor, $\mathbf{A}_N$ and g_{nN} represent the hyperfine tensors and the nuclear g factor of the ^{14}N ($I_N = 1$), respectively; $\mathbf{A}_i$ and g_{ni} represent the hyperfine tensor and nuclear g factor of nucleus i, respectively, for the ^{13}C ($I = 1/2$) and ^{29}Si ($I = 1/2$) nuclear spins; $\mathbf{P}_N$·is the quadrupole tensor of the ^{14}N nuclear spin.

Figure 9b shows the ESE-detected ^{29}Si and ^{13}C ENDOR spectra on the high-frequency side of the ^{29}Si and ^{13}C nuclear Larmor frequencies (indicated by arrows) in 4H-SiC and 6H-SiC for $B \| c$ at 1.2 K and 95 GHz. The upper spectra belong to the N donor substituting carbon on a cubic-like sites in 6H-SiC. The middle spectrum was measured in 6H-SiC at N position k1 in the EPR spectrum (partially overlaps with h position). The lower spectrum, 4H, k, belongs to the N donor in k site in 4H-SiC. The ^{29}Si k1, k2 site lines are both marked by squares, the positions of the h site lines are marked by circles. The ^{13}C positions of the *h* site lines are marked by open circles, those of the k1 site lines by squares and those of the k2 site by triangles. The orientational dependence of the ^{29}Si ENDOR lines (experimental data points marked by diamonds) of the k site in 4H-SiC in the (11–20) or (xz) plane is presented. The spectra have been corrected for the shift of the nuclear Larmor frequency with respect to the orientation $B \| c$ ($\theta = 0°$).

From the comparison between the ^{29}Si and ^{13}C ENDOR spectra for the different sites in 4H-Si^{13}C and 6H-Si^{13}C in Fig. 9b one can see, that the spin density distribution of the N-donor electron over the ^{13}C and ^{29}Si nuclei differs between 4H-SiC and 6H-SiC. Whereas the main part of the spin density is localized on the ^{29}Si atoms for the k site in 4H-SiC (as expected for a donor electron) it is localized mainly on the ^{13}C atoms for the h and cubic-like sites in 6H-SiC. Note also, that the spectrum of 6H-SiC contains more lines around the ^{13}C nuclear Larmor frequency than the spectrum of 4H-SiC around either the ^{13}C or ^{29}Si nuclear Larmor frequency. The horizontal arrows in Fig. 9b indicate the maximum values of the ^{29}Si ENDOR lines in 6H-SiC and ^{13}C ENDOR lines in 4H-SiC.

There are three major factors determining HF interactions for shallow donors in SiC crystal, which is indirect-gap semiconductors: (i) smoothly decreasing of HF interactions with increasing distance from the donor; (ii) the spin density

localization on atoms, which is characterized by dimensionless gain coefficients; and (iii) interference effects originating from the existence of several valleys in these semiconductors, which destroys the smooth falloff of HF interactions on atoms with distance. Incidentally, this interference effect considerably complicates the interpretation of EPR and ENDOR spectra in indirect-gap semiconductors, unlike in direct-gap semiconductors (ZnO, AgCl, AlN), in which HF and SHF interactions have been assigned with a high degree of confidence (see Sects. 2, 3, 5).

In total more than fifteen groups of nuclei were identified in Ref. [47] together with the corresponding HF tensors and the Euler angles. After the addition results of new studies [48–54] where strong HF interactions with the two Si and C shells were directly observed in the EPR spectra, the number of shells that have been identified in ENDOR studies was revised. Thus the maximum constants, which are registered in the ENDOR spectra were now attributed to the third shell, instead of the first one.

The almost isotropic HF structure for nitrogen donors in quasi-cubic positions (k) due to the HF interaction with one Si atom was directly observed in EPR spectra in 4H-SiC and 6H-SiC crystals. The surrounding ions of the Nk SD in 4H-SiC, for which the HF interactions resolved by EPR and ENDOR are presented in Fig. 10. Figure 10 shows a schematic representation of the crystal structure around the k site in 4H-SiC. The direction of the c-axis is shown, the staircase drawn with the heavy lines. In the bottom, the orientation of the x, y, z axes are indicated. The {11–20} plane, contains the c-axis (z), x-axis and run parallel to the surface of the paper. The N atom in C position is indicated. The Roman numbers placed near the nuclei correspond to the numbers indicating the different groups. The surrounding of the k1-site in 6H-SiC is exactly the same as the surrounding of the k site in 4H-SiC.

We will only consider the shells formed by Si and C atoms, labeled by I, Ia, II, IIa, III, IIIa, IIIb and IIIc. The HF structure of the first shell (one Si atom labeled I) and three carbon atoms of the second shell (labeled IIb) were resolved in the EPR spectra. The HF structure and unpaired electron density outside these shells were analyzed in Ref. [47]. Almost isotropic hyperfine splitting, caused by interaction with one Si atom in the first shell, labeled I (Fig. 10), is the next: 1.46 mT (41 MHz) in 4H-SiC and 0.96 mT (26.9 MHz) in 6H-SiC.

The isotropic HF splitting of ^{13}C which was observed in the EPR spectra as satellites in ^{29}Si depleted crystals for Nk1 and Nk2 in 6H-SiC and Nk in 4H-SiC. We refer these EPR signals to the interaction with three carbon atoms, labeled by IIb, that bound along c-axis to three silicon nucleus labeled by Ia (see Fig. 10). This isotropic HF splitting is 0.6 mT (16.8 MHz) for 4H-SiC and 0.5 mT (14 MHz) for 6H-SiC. The corresponding spin density on one Si atom in 4H-SiC and 6H-SiC are 0.89% and 0.6%, respectively, and those on each of the three C atoms in 4H-SiC and 6H-SiC are 0.44% and 0.37%, respectively. Anisotropic HF interaction with three silicon atoms in the first shell located in the basal plane which are labeled Ia from ENDOR data [3] are: $a = 6.54$ MHz, $b = 1.26$ MHz, $b' = 0.75$ MHz, $s = 0.14\%$, $p = 1.1\%$. Thus, in 4H-SiC, the total degree of localization of the unpaired electron on the central N atom and in the first coordination shell (containing four Si atoms I and Ia, Fig. 10) should be 7.4%. We should add to this about 2% for the assumed three C atoms of the second shell. Thus, the total spin density within the first two
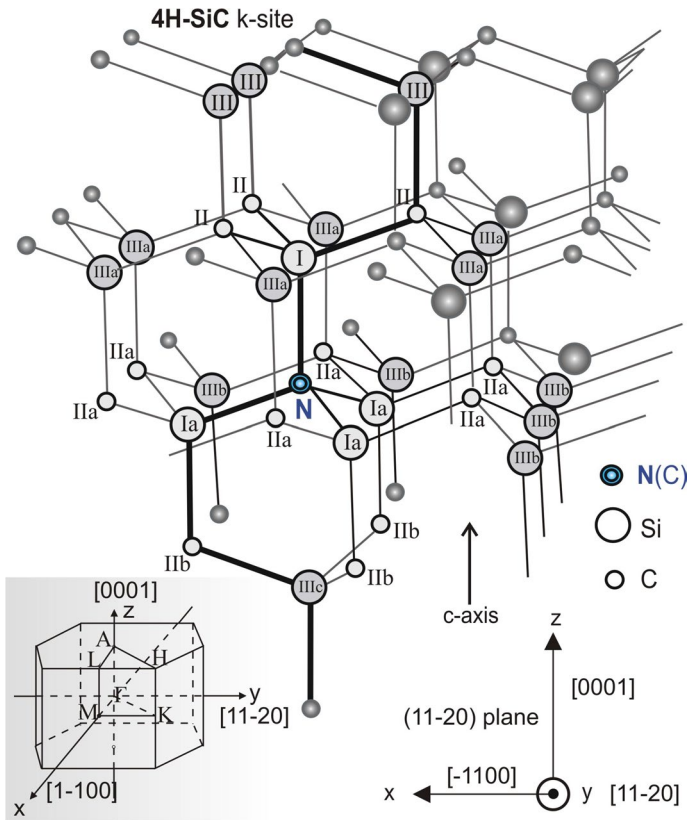
Fig. 10 A schematic representation of the crystal structure around the k site in 4H-SiC. The direction of the c-axis is shown, the staircase drawn with the heavy lines. At the bottom, the orientation of the *x*, *y*, *z* axes are indicated. The {11–20} plane, contain the *c*-axis (*z*), *x*-axis and run parallel to the surface of the paper. The N atom in C position is indicated. The Roman numbers placed near the nuclei correspond to the shell numbers. The surrounding of the k1-site in 6H-SiC is exactly the same as the surrounding of the k site in 4H-SiC. (inset) The reciprocal lattice of 4H-SiC and 6H-SiC with lattice parameters $4\pi/(\sqrt{3}a)$ (distance from the center of the hexagon to a corner) and $2\pi/c$ (hight of the hexagon). The lattice is rotated by 60° around the c-axis with respect to the lattice in real space. The positions of the special symmetry points are shown, together with the orientation of the hexagon with respect to the crystallographic axis system, *x*, *y*, and *z* in real space. The Γ point is the center of the hexagon. The M point lies in the (11–20) plane, the K point in the (− 1100) plane and the L point lies above the *M* point along the [0001] direction

coordination shells is approximately 9.5%. For 6H-SiC, the respective quantities should be about 1.5 times lower.
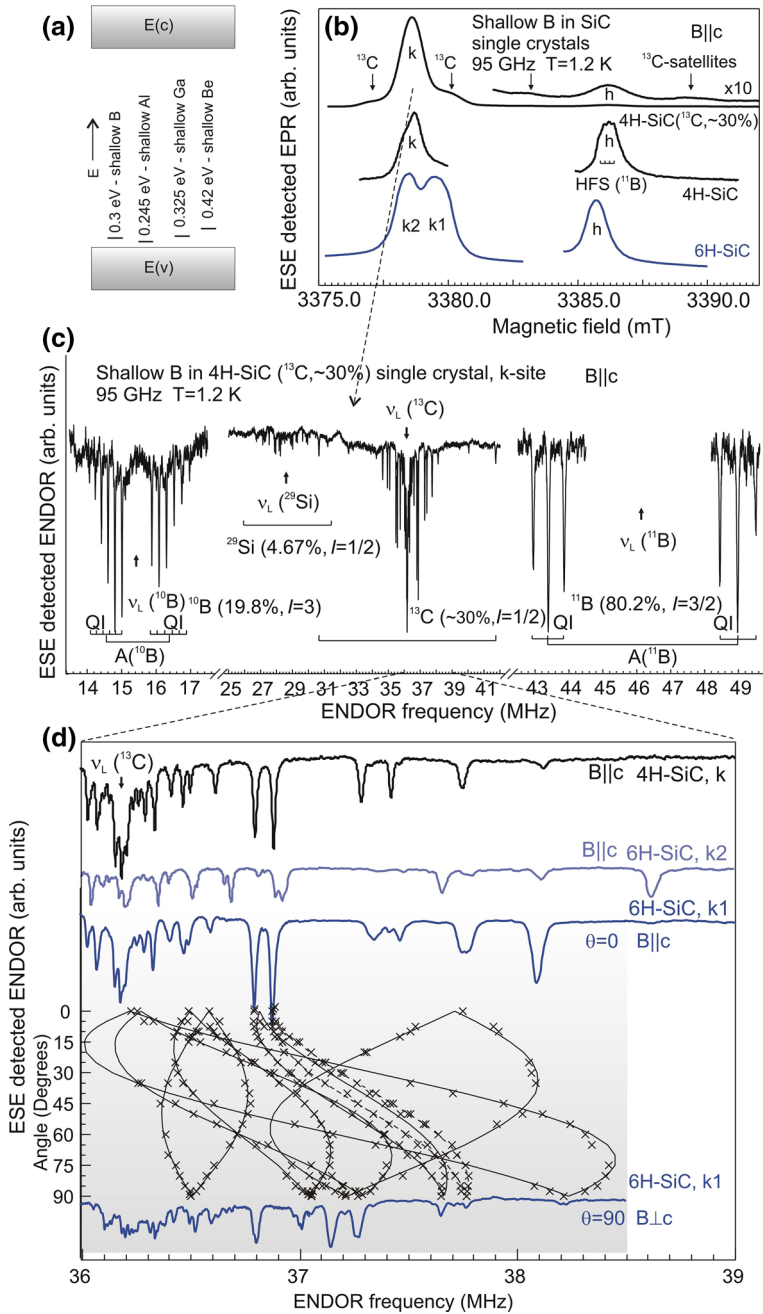
These values should be added to those obtained in an ENDOR study [47], which must be corrected by the including of the strong HF interactions for the nitrogen k positions, which were resolved in the EPR spectra. In 4H-SiC, according to ENDOR studies there are strongest HF interactions with C atoms in two groups: with $a = 5.02$ MHz ($s = 0.13\%$) and with $a = 4.4$ MHz and $b = 0.23$ MHz ($s = 0.12\%$ and $p = 0.22\%$). These HF interactions can be

attributed to the C atoms labeled as II (3 atoms) and IIa (6 atoms) in Fig. 10.
In 4H-SiC, according to ENDOR studies the strongest HF interactions with Si
atoms in two groups: with $a = 4.8$ MHz ($s = 0.1\%$), $b = 0.04$ MHz ($p = 0.04\%$);
and with $a = 4.14$ MHz and $b = 0.34$ MHz ($s = 0.09\%$ and $p = 0.3\%$) with bonds
along c-axis can be attributed to the Si atoms labeled as III and IIIc. For IIIa
and IIIb Si groups (Fig. 10) located in the basal plane HF interactions are the
next: $a = 2.3$ MHz ($s = 0.05\%$), $b = 0.31$ MHz ($p = 0.27\%$) and $a = 2.0$ MHz
($s = 0.04\%$), $b = 0.12$ MHz ($p = 0.11\%$).

The spin density corresponding to the observed ENDOR lines is p like in char-
acter and located mainly on the Si atoms for the *k* site in 4H-SiC, whereas for the
three sites in 6H-SiC the spin density is s-like in character and located mainly on the
C atoms. An explanation for the difference in the electronic wave function of the N
donor in 4H-SiC and 6H-SiC can be found in the large difference in the band struc-
ture of the two polytypes and in the position of the minima in the Brillouin Zone.
As a result, the linear combination of atomic orbitals describing the wave function
of the donor electron is different. The ENDOR and EPR results are consistent with
mainly Si-like conduction-band minima in 4H-SiC and C-like conduction-band min-
ima in 6H-SiC.

The conduction band minimum in the 4H-SiC polytype is at point *M*, whereas
that in 6H-SiC is located between points *M* and *L*, at a relative distance of approxi-
mately 60% from point M (see inset in Fig. 10). The band structures are such that
the effective masses in the plane perpendicular to the c axis are approximately the
same for both polytypes ($m_\perp = 0.445\ m_0$ for 4H-SiC and $m_\perp = 0.43\ m_0$ for 6H-SiC)
while differing noticeably along the c axis. Indeed, for 4H-SiC, the effective mass
along the c axis is $m_\parallel = 0.32\ m_0$, whereas for 6H-SiC we have $m_\parallel = 1.7\ m_0$. Thus,
for the 4H-SiC polytype, the electron wave function is very nearly spherically sym-
metric, while for 6H-SiC the electron wave function is contracted noticeably along
the c axis, i.e., is pancake-shaped. The effective Bohr radius of the electron wave
function is $a^* = 13$ Å for 4H-SiC, and $a^* = 7.2$ Å for 6H-SiC and the corresponding
shallow-donor ionization energies E_{eff} are 47 meV for 3C-SiC, 54 meV for 4H-SiC,
and 101 meV for 6H-SiC.

(a)

E(c)

E $\longrightarrow$

| 0.3 eV - shallow B

| 0.245 eV - shallow Al

| 0.325 eV - shallow Ga

| 0.42 eV - shallow Be

E(v)

(b) ESE detected EPR (arb. units)

Shallow B in SiC single crystals
95 GHz T=1.2 K

B||c

^{13}C k ^{13}C ^{13}C-satellites

↓   ↓   ↓   ↓   ↓   x10

h

4H-SiC(^{13}C,~30%)

k   h

HFS (^{11}B)   4H-SiC

k2 k1   h   6H-SiC

Magnetic field (mT)

3375.0   3380.0   3385.0   3390.0

(c) ESE detected ENDOR (arb. units)

Shallow B in 4H-SiC (^{13}C,~30%) single crystal, k-site   B||c
95 GHz T=1.2 K

ν_L (^{13}C)
↓

↑

ν_L (^{29}Si)

^{29}Si (4.67%, I=1/2)

ν_L (^{10}B) ^{10}B (19.8%, I=3) ^{13}C (~30%,I=1/2)

↑

ν_L (^{11}B)

^{11}B (80.2%, I=3/2)

QI   QI   QI   QI

A(^{10}B)   A(^{11}B)

ENDOR frequency (MHz)

14 15 16 17   25 27 29 31 33 35 37 39 41   43 44 45 46 47 48 49

(d) ESE detected ENDOR (arb. units)

ν_L (^{13}C)
↓

B||c 4H-SiC, k

B||c 6H-SiC, k2

6H-SiC, k1

θ=0   B||c

Angle (Degrees)

0
15
30
45
60
75
90

6H-SiC, k1

θ=90 B⊥c

ENDOR frequency (MHz)

36   37   38   39

6.2 Shallow Acceptors in SiC

The group-III elements B, Al and Ga are the most important acceptor impurities in

SiC. These impurities can be introduced during the growth or afterwards by diffusion or by implantation. A substitutional atom of a group-III element normally acts as an acceptor in SiC since there is a deficit of one valence electron to complete the normal tetrahedral bonding. At sufficiently low temperatures the hole is localized near the acceptor atom; at high temperatures, it can ionize and give rise to p-type conduction. The experimental energy levels of group-III shallow acceptors are summarized in Fig. 11a.

EPR spectra of shallow B were studied in 3C-, 4H- and 6H polytypes of B-doped SiC [55–63]. B has two stable isotopes, ^{10}B (natural abundance 19.8%, $I = 3$) and ^{11}B (80.2%, $I = 3/2$).

Figure 11b shows three 95-GHz EPR spectra of the sB acceptor in SiC with $B \| c$ axis. The upper spectrum is obtained in 4H-SiC single crystal (^{13}C enriched) and consists of two lines; one is related to a B atom on a cubic-like position (k) in the crystal, the other is related to a B atom on a hexagonal position (h), the weakness of the h signal is caused by the position of the Fermi level. The weak satellites in the magnified spectrum are caused by the HF interaction with the nearest-neighboring ^{13}C nucleus. The middle spectrum was measured on a 4H-SiC single crystal with ^{13}C natural abundance. We remark that owing to the small linewidth of the sB signals, the HF interaction with the B nuclear spin is visible in this spectrum on the sB line related to the h site. The lowest spectrum is obtained under similar conditions on the 6H-SiC crystal (^{13}C enriched) and ^{11}B isotope doped. The three lines marked with k1, k2, and h correspond to the two cubic-like sites and the hexagonal site of the sB acceptor.

The values of the g-tensor along the principal axes were measured in different polytypes of SiC to be: g_z ($g_\|$) $= 2.0020$ and g_x, g_y ($g_\perp$) $= 2.006$, where the local z-axis coincides with one of the direction Si–C (for h-site it is c-axis of the crystal, for k1 or k2—site it is one of six nonequivalent Si–C directions, which is not coincide with c-axis. x and y axes are in a plane perpendicular to the z axis and x axis lies in one of the {11–20} planes in 6H-SiC (4H-SiC). Thus, the g-tensor of shallow B centres is almost axial around the local z-axis for all shallow B centres in SiC. g-factor along z-axis was shown to be practically equal to the value g of the free electron spin. The HF interaction tensor A reflects the axial symmetry of the shallow B centre along the local z-axis. For cubic-like positions, "nonaxial" defect, there is small deviation from axial symmetry, which only reflects the influence of crystal field along c-axis and seems to be not important for the understanding of the structure of shallow B.

A high-frequency pulsed EPR and ENDOR study has been carried out on the shallow boron acceptor in natural and ^{13}C isotope enriched 4H-SiC and 6H-SiC [59, 60]. From the HF interaction of the electron spin $S = 1/2$ with the ^{13}C ($I = 1/2$) nuclei the spatial distribution of the electronic wave function has been established. It is found that there are subtle differences in the degree of localization of this wave function between the different sites—cubic-like and hexagonal in the two polytypes 4H-SiC and 6H-SiC. In particular, it is found that the spatial distribution is highly anisotropic. This anisotropy can be rationalized by considering the anisotropy of the hole mass, i.e., by assuming that effective-mass theory is (partly) valid in describing the remote part of the spatial distribution of the electronic wave function.

Figure 11c shows an overview of the total ENDOR spectrum as measured on the 4H-Si^{13}C sample with a natural abundance of B with $B \| c$. The figure is a nice example of the spectral resolution that can be obtained at high-frequency ENDOR. As the sample is ^{13}C enriched, the ENDOR lines for this isotope are very intense. Only for the outer ^{13}C ENDOR lines there is some overlap with the ^{29}Si and ^{11}B lines. Arrows indicate the Larmor frequency of the relevant isotopes in the fields in which the EPR signals (Fig. 11b) were measured.

Figure 11d shows part of the ^{13}C ENDOR spectra of the sB k1 and k2 site in 6H-Si^{13}C:^{11}B crystal and the k site in 4H-Si^{13}C crystal. Note, that the k1 spectrum in 6H-SiC is the same, except intensities, as that of the k site in 4H-SiC. This is the case for all measured orientations, which leads us to the conclusion that these two centers have the same position and thus the same surrounding in the crystal. We thus assign the corresponding EPR line to the k1 site, as this site is situated at a similar crystal position as the k site in 4H-SiC. Moreover, these two sites have the same environment in the two layers perpendicular to the c axis above and below the B center, which we used in the assignment of the ENDOR lines. The EPR line with the smallest g-tensor anisotropy was assigned to the site closest to the h site, as the g tensor of the hexagonal site is axial. As it will turn out, the spin density distribution is not isotropic. The spectrum of k2 contains less lines around the carbon nuclear Larmor frequency than that of k1 which, combined with the fact that we found one more line at 45 MHz for k2, suggests that for k2 the spin density is more localized than for k1. Above the k2 ENDOR spectrum, a rescaled part of the k1 spectrum is shown for comparison, from which it can seen that the ENDOR lines belonging to the k1 site are also weakly present in the k2 ENDOR spectrum. Very weakly, the strongest k2 lines can also be seen in the k1 spectrum. This ''crosstalk'' is the result of the small overlap of the EPR lines of the k1 and k2 sites in 6H-SiC. In the bottom of Fig. 11d the angle dependence of the HF interaction of the ^{13}C nuclei for the k1 site in 6H-SiC is shown.

The most remarkable result of the ENDOR study is the assignment of lines in the ^{13}C ENDOR spectra to specific C atoms up to eleven bond lengths away from the B atom. This allows for a determination of the spatial distribution of the unpaired spin density of the sB acceptor, and in particular of an investigation of the difference in the electronic properties of the cubic-like and hexagonal sites in 4H-SiC and 6H-SiC. To visualize the delocalization of the electronic wave function, for example, connected to the k1 site, we show in Fig. 12a in the form of a contour plot its spin density at C atoms in the main (11–20) plane, that is, the plane containing the c axis [60]. The crystal can be regarded as a collection of staircases along the c axis. The staircase on which the B and the main C are situated is indicated as a full line in. The next staircases are located in the one step up and one step down (11–20) planes, are projected onto the plane on which the B and the main C are situated, and are indicated by a dotted line. It is seen that the electron density is distributed in an ellipsoidal shape with the main symmetry axis making an angle of 70° with the c axis, i.e., along the direction of the B-main C line.

A model of shallow B in h and k sites is presented in Fig. 12b, where a direction of the off-center shift of B atom corresponds to the local z-axis. Double arrow shows off-center shift of C atom with main spin density.
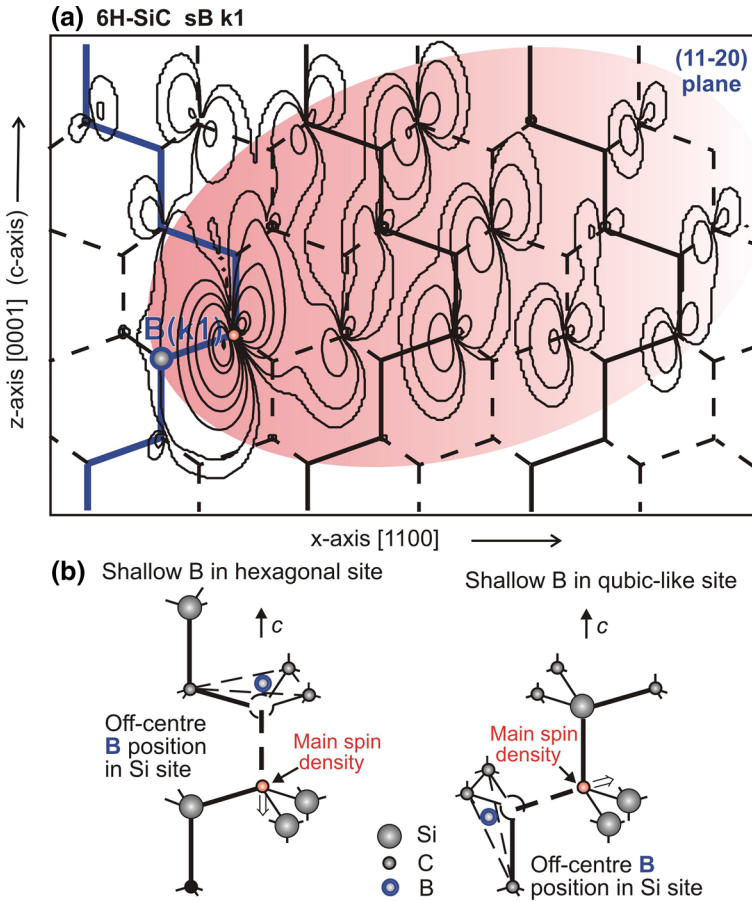
Fig. 12 a The value of the square of the wave function of the 6H-SiC k1 site in the (11–20) plane, containing the B atom in Si position and the C atom with the largest spin density is shown as a function of the position in the xz plane using a contour plot. Each line indicates a certain height and the larger the amount of lines the higher is the peak. The B position is indicated. The position of the main C atom can be recognized from the large number of contour lines. The full lines indicate the c axes located in the (11–20) plane, containing the B atom and the main C atom, and the dotted lines indicate the projection of the axes located in the ± 1 planes into the main plane. It is clear that the spin density is very anisotropic. The distribution points away from the B atom into one direction only along the B–C connection line, making an angle of 70° to the c axis. The nuclei on the other side of the B atom carry an almost negligible amount of spin density. **b** A model of shallow B in h and k sites. The direction of off-center shift of B atom corresponds to the local z-axis. Double arrow shows off-center shift of C atom with main spin density

All three sB centers in 6H-SiC were shown to have different localizations of the spin density and thus different ionization energies. The question arises whether the anisotropic distribution of the electronic wave function on the remote ^{13}C nuclei as revealed by the ^{13}C ENDOR data can be rationalized on the basis of effective-mass theory (EMT) [20]. Shallow aluminum (sAl) and shallow gallium (sGa), in contrast to sB, (see Fig. 11a) show a highly anisotropic g-tensor in agreement with

the calculated g anisotropy of the valence-band hole. In the case of the sB acceptor the orbital angular momentum is quenched, and one would not expect to see band-structure properties reflected in the properties of the hole attached to the sB acceptor. Nevertheless, we observe that the electronic wave function of the quasi-cubic sB acceptor perpendicular to the c axis extends considerably further than parallel to the c axis, in agreement with the anisotropy of the hole mass: $m_{h\parallel} = 1.67\ m_e$ and $m_{h\perp} = 0.62\ m_e$. Here we remark that the anisotropy in the perpendicular plane is averaged out at higher temperatures, where it is known that the B-main C bond starts to jump between the three possible directions of this bond. The cylindrically symmetric spin density so obtained spreads out further in the perpendicular plane than along the c axis.

In conclusion, the unique capabilities of pulsed ENDOR methods for monitoring the spatial distribution of wave functions of centers with shallow levels in a number of wide-gap semiconductors belonging to different groups of compounds, such as I–V, II–VI, III–V, IV–IV, have been demonstrated. Physical effects are given that are caused by the delocalization of electrons in such systems, such as hyperfine interactions in the region of electron delocalization, confinement effects in nanostructures, dynamic polarization of nuclei in crystals and based quantum dots, processes of negative U with DX-relaxation of shallow impurities, and finally, the establishment of the electronic structure of intrinsic and impurity centers, obtaining information on the structure of excitons.

References

1. Y.N. Molin, K.M. Salikhov, K.I. Zamaraev, *Spin Exchange* (Springer, Berlin, 1980)
2. K. Möbius, A. Savitsky, *High-Field EPR Spectroscopy on Proteins and Their Model Systems* (RSC Publishing, London, 2009)
3. J.A.J.M. Disselhorst, H.J. van der Meer, O.G. Poluektov, J. Schmidt, J. Magn. Reson. A **115**, 183 (1995)
4. H. Blok, J.A.J.M. Disselhorst, H. van der Meer, S.B. Orlinskii, J. Schmidt, J. Magn. Res. **173**, 49 (2005)
5. W.B. Mims, Chapter 4, in *Electron Paramagnetic Resonance*. ed. by S. Geschwind (Plenum, New York, 1972), pp. 263–351
6. P.G. Baranov, S.B. Orlinskii, C. de Mello Donegá, J. Schmidt, Appl. Magn. Reson. **39**, 151 (2010)
7. S.B. Orlinskii, J. Schmidt, P.G. Baranov, D.M. Hofmann, C. de Mello Donegá, A. Meijerink, Phys. Rev. Lett. **92**, 047603 (2004)
8. D.M. Hofmann, H. Zhou, D.R. Pfisterer, H. Alves, B.K. Meyer, P. Baranov, N. Romanov, C. de Mello Donegá, A. Meijering, S. Orlinskii, H. Blok, J. Schmidt, Phys. Stat. Sol. **1**, 908 (2004)
9. S.B. Orlinskii, J. Schmidt, E.J.J. Groenen, P.G. Baranov, C. de Mello Donegá, A. Meijerink, Phys. Rev. Lett. **94**, 097602 (2005)
10. S.B. Orlinskii, H. Blok, E.J.J. Groenen, J. Schmidt, P.G. Baranov, C. de Mello Donegá, A. Meijerink, Magn. Reson. Chem. **43**, S140–S144 (2005)
11. S.B. Orlinskii, H. Blok, J. Schmidt, P.G. Baranov, C. de Mello Donegá, A. Meijerink, Phys. Rev. B **74**, 045204 (2006)

12. S.B. Orlinskii, J. Schmidt, P.G. Baranov, D. Rauh, V. Lorrmann, V. Dyakonov, Phys. Rev. B **77**, 115334 (2008)
13. S.B. Orlinskii, J. Schmidt, P.G. Baranov, C. de Mello Donegá, A. Meijerink, Phys. Rev. B **79**, 165316 (2009)
14. D.M. Hofmann, A. Hofstaetter, F. Leiter, H. Zhou, F. Henecker, B.K. Meyer, S.B. Orlinskii, J. Schmidt, P.G. Baranov, Phys. Rev. Lett. **88**, 045504 (2002)
15. H. Blok, S.B. Orlinski, J. Schmidt, P.G. Baranov, Phys. Rev. Lett. **92**, 047602 (2004)
16. Yu.S. Kutin, G.V. Mamin, S.B. Orlinskii, A.P. Bundakova, P.G. Baranov, JETP Lett. **95**, 471 (2012)
17. P.G. Baranov, H.J. von Bardeleben, F. Jelezko, J. Wrachtrup, *Magnetic Resonance of Semiconductors and Their Nanostructures: Basic and Advanced Applications: Springer Series in Materials Science*, vol. 253 (Springer, Austria, 2017)
18. C.G. Van de Walle, Phys. Rev. Lett. **85**, 1012 (2000)
19. M.T. Bennebroek, J. Schmidt, J. Magn. Reson. **128**, 199 (1997)
20. A.M. Stoneham, *Theory of Defects in Solids* (Clarendon Press, Oxford, 1975)
21. M.T. Bennebroek, O.G. Poluektov, A.J. Zakrzewski, P.G. Baranov, J. Schmidt, Phys. Rev. Lett. **74**, 442 (1995)
22. M.T. Bennebroek, A. Arnold, O.G. Poluektov, P.G. Baranov, J. Schmidt, Phys. Rev. B **54**, 11276–11289 (1996)
23. M.C.J.M. Donckers, O.G. Poluektov, J. Schmidt, P.G. Baranov, Phys. Rev. B **45**, 13061–13063 (1992)
24. O.G. Poluektov, M.C.J.M. Donckers, P.G. Baranov, J. Schmidt, Phys. Rev. B **47**, 10226–10234 (1993)
25. M.T. Bennebroek, A. Arnold, O.G. Poluektov, P.G. Baranov, J. Schmidt, Phys. Rev. B **53**, 15607–15616 (1996)
26. N.G. Romanov, P.G. Baranov, Semicond. Sci. Technol. **9**, 1080 (1994)
27. P.G. Baranov, N.G. Romanov, Appl. Magn. Reson. **21**, 165 (2001)
28. L. Landau, Phys. Z. Sowjet. Un. **3**, 664 (1933)
29. M. Höhne, M. Stasiw, Phys. Status Solidi **28**, 247 (1968)
30. M.T. Bennebroek, A.V. Duijn-Arnold, J. Schmidt, O.G. Poluektov, P.G. Baranov, Phys. Rev. B **66**, 054305 (2002)
31. K.S. Song, R.T. Williams, *Self-Trapped Excitons* (Springer, Berlin, 1993)
32. B.S. Gourary, F.J. Adrian, Phys. Rev. **105**, 1180–1192 (1957)
33. R.A. Zhitnikov, P.G. Baranov, N.I. Melnikov, Phys. Status Solidi (b) **59**, K111 (1973)
34. R.C. Baetzold, R.S. Eachus, J. Phys. Condens. Matter. **7**, 3991 (1995)
35. S. Sakuragi, H. Kanzaki, Phys. Rev. Lett. **38**, 1302–1305 (1977)
36. A.W. Overhauser, Phys. Rev. **89**, 689 (1953)
37. G. Denninger, D. Reiser, Phys. Rev. B **55**, 5073 (1997)
38. V. Dyakonov, G. Denninger, Phys. Rev. B **46**, 5008 (1992)
39. B. Monemar, P.P. Paskov, J.P. Bergman, A.A. Toropov, T.V. Shubina, Phys. Status Solidi B **244**, 1759–1768 (2007)
40. G.A. Baraff, E.O. Kane, M. Schluter, Phys. Rev. Lett. **43**, 956–959 (1979)
41. G.D. Watkins, J.R. Troxell, Phys. Rev. Lett. **44**, 593–596 (1980)
42. D.J. Chadi, K.J. Chang, Phys. Rev. Lett. **61**, 873–876 (1988)
43. S.B. Orlinskii, J. Schmidt, P.G. Baranov, M. Bickermann, B.M. Epelbaum, A. Winnacker, Phys. Rev. Lett. **100**, 256404 (2008)
44. A. Abragam, B. Bleaney, *Electron Paramagnetic Resonance of Transition Ions* (Oxford University Press, Oxford, 1970)
45. E.N. Kalabukhova, N.N. Kabdin, S.N. Lukin, Sov. Phys. Solid State **29**, 8 (1987)
46. S. Greulich-Weber, M. Feege, J.-M. Spaeth, E.N. Kalabukhova, S.N. Lukin, E.N. Mokhov, Solid State Commun. **93**, 393 (1995)
47. A.V. Duijn-Arnold, R. Zondervan, J. Schmidt, P.G. Baranov, E.N. Mokhov, Phys. Rev. B **64**, 085206 (2001)
48. N.T. Son, E. Janzen, J. Isoya, S. Yamasaki, Phys. Rev. B **70**, 193207 (2004)
49. K. Szász, X.T. Trinh, N.T. Son, E. Janzén, A. Gali, J. Appl. Phys. **115**, 073705 (2014)
50. D.V. Savchenko, E.N. Kalabukhova, V.S. Kiselev, J. Hoentsch, A. Poppl, Phys. Status Solidi B **246**, 1908 (2009)
51. D.V. Savchenko, E.N. Kalabukhova, A. Poppl, B.D. Shanina, Phys. Status Solidi B **249**, 2167 (2012)

52. P.G. Baranov, B.Y. Ber, O.N. Godisov, I.V. Il'in, A.N. Ionov, E.N. Mokhov, M.V. Muzafarova, A.K. Kaliteevskii, M.A. Kaliteevskii, P.S. Kop'ev, Phys. Solid State **47**, 2219 (2005). (**Fizika Tverdogo Tela 47, 2127 (2005)**)

53. N.T. Son, J. Isoya, T. Umeda, I.G. Ivanov, A. Henry, T. Ohshima, E. Janzén, Appl. Magn. Reson. **39**, 49–85 (2010)

54. M.V. Muzafarova, I.V. Il'in, A.N. Anisimov, E.N. Mokhov, V.A. Soltamov, P.G. Baranov, Phys. Solid State **58**, 2406 (2016). (**Fizika Tverdogo Tela 58, 2319 (2016)**)

55. H.H. Woodbury, G.W. Ludwig, Phys. Rev. **124**, 1083 (1961)

56. A.G. Zubatov, I.M. Zaritskii, S.N. Lukin, E.N. Mokhov, V.G. Stepanov, Sov. Phys. Solid State **27**, 197 (1985)

57. N.P. Baran, V.Y. Bratus', A.A. Bugai, V.S. Vikhnin, A.A. Klimov, V.M. Maksimenko, T.L. Petrenko, V.V. Romanenko, Phys. Solid State **35**, 1544 (1993).

58. P.G. Baranov, *Acceptor Impurities in Silicon Carbide: Electron Paramagnetic Resonance and Optically Detected Magnetic Resonance Studies, Defect and Diffusion Forum*, vol. 148–149 (Scitec Publications, Switzerland, 1997), pp. 129–160

59. T. Matsumoto, O.G. Poluektov, J. Schmidt, E.N. Mokhov, P.G. Baranov, Phys. Rev. B **55**, 2219 (1997)

60. A. van Duijn-Arnold, J. Mol, R. Verberk, J. Schmidt, E.N. Mokhov, P.G. Baranov, Phys. Rev. B **60**, 15829 (1999)

61. A.V. Duijn-Arnold, T. Ikoma, O.G. Poluektov, P.G. Baranov, E.N. Mokhov, J. Schmidt, Phys. Rev. B **57**, 1607 (1998)

62. A. van Duijn-Arnold, J. Schmidt, O.G. Poluektov, P.G. Baranov, E.N. Mokhov, Phys. Rev. B **60**, 15799 (1999)

63. I.V. Ilin, Y.A. Uspenskaya, D.D. Kramushchenko, M.V. Muzafarova, V.A. Soltamov, E.N. Mokhov, P.G. Baranov, Phys. Solid State **60**, 644 (2018)

Authors and Affiliations

S. B. Orlinskii[1] · V. A. Soltamov[2] · G. V. Mamin[1] · O. G. Poluektov[3] · J. Schmidt[4] · P. G. Baranov[2]

✉ V. A. Soltamov
victrosoltamov@gmail.com

1. Federal Center of Shared Facilities of Kazan State University, 420008 Kazan, Russia

2. Ioffe Institute, 194021 Saint Petersburg, Russia

3. Chemical Sciences and Engineering Division, Argonne National Laboratory, Lemont, IL 60439, USA

4. Huygens Laboratory, Leiden University, Leiden, The Netherlands